International Journal of Heat and Mass Transfer 220 (2024) 124957

Contents lists available at ScienceDirect

International Journal of Heat and Mass Transfer

journal homepage: www.elsevier.com/locate/ijhmt

Thermite-for-Demise (T4D): Experimental analysis of heat transfer principles and preliminary sizing of an application

A. Finazzi, P. Finocchi, S. Carlotti, F. Maggi *

Politecnico di Milano, Milano, MI, 20156, Italy

ARTICLE INFO

Keywords:
Thermite
Re-entry
Spacecraft demise
Mechanical activation
Genetic algorithm

ABSTRACT

The use of exothermic reactions to aid satellite demise during re-entry is under investigation. An energetic material, if stored on board, could passively ignite thanks to the heat load experienced by the spacecraft during re-entry, and ease its complete ablation. Thermites are good candidates for this application because of their high energy density and relative stability. Their effectiveness is strictly related to the heat transfer efficiency between the ignited powder and its confining vessel. Experiments in non-relevant environment were conducted for Al+Fe_2O_3 thermite to quantify this value. The average heat transfer efficiency was quantified at 60%, with respect to the theoretical heat release of the mixture. A novel numerical model implementing a T4D application, named TRANSIT (TRANsatmosferic SImulation Tool), is presented and verified with respect to two commercial software packages. In particular, literature data for SAM and dedicated simulations for SCARAB have been used in this phase. TRANSIT is then employed to preliminarily size a thermite charge to aid spacecraft demise during re-entry for three simple re-entering objects. A genetic algorithm is employed to optimize the thermite to spacecraft mass ratio, assuring complete demise.

1. Introduction

The annual report on the space environment by the European Space Agency (ESA) [1] has been registering an exponential increase in the number of active satellites since several years. The trend is expected to be maintained in the future. It is estimated that the number of objects to be launched in the next three years will be higher than the one reached in the last six decades [2].

Actually, the situation is more complex because a significant share of satellite population has already demonstrated not to be compliant, in part or in full, with the international guidelines [3]. The situation for the 2010-2020 decade, described in the ESA's Annual Space Environment Report 2022 [1], can be an example. The document reported that, for the spacecrafts which mass is more than 1000 kg, the 18% is compliant with the 25 years-rule, but not with the limit for the ground casualty risk. Therefore, the effort to improve spacecraft End-of-Life management is of paramount importance. For the Low Earth Orbit (LEO), the main countermeasure to limit overcrowding is to assure the re-entry of the spacecraft in due time, after the end of its operative life.

An uncontrolled re-entry is beneficial in terms of fuel budget, but it does not allow a proper control over the ground footprint. Vice versa, a controlled re-entry is rather expensive in terms of fuel (up to 4-5 times the propellant on board [4]) but mitigates the casualty risk on ground. This contrast is reminded also by international guidelines [3] which call for no uncontrolled re-entry with a casualty risk higher than 10^{-4}, and for no fragments reaching the ground with energy higher than 15 J.

The field of research to limit the casualty risk and let uncontrolled re-entries become more and more common is named Design-for-Demise (D4D). In particular, the casualty risk on ground can be limited either by promoting the ablation of the satellite or by limiting the ground footprint. Currently, the main explored strategies focus on minimizing the required heat for complete ablation, optimizing heat transfer to the structure, or minimizing the casualty risk area on ground. In addition, a rather unexplored possibility consists of maximizing the available heat reaching target parts of the satellite during re-entry.

In this last group of methods, the Thermite-for-Demise (T4D) approach is now under investigation. This strategy considers an extra source of enthalpy on board (the thermite pyrotechnic charge) to be activated during the re-entry. The additional heat could aid the space-

* Corresponding author.
E-mail addresses: alessandro.finazzi@polimi.it (A. Finazzi), piero.finocchi@mail.polimi.it (P. Finocchi), stefania.carlotti@polimi.it (S. Carlotti), filippo.maggi@polimi.it (F. Maggi).

https://doi.org/10.1016/j.ijheatmasstransfer.2023.124957
Received 29 August 2023; Received in revised form 19 October 2023; Accepted 11 November 2023
Available online 4 December 2023

craft to complete its demise, in combination with the heat flux naturally experienced during the re-entry process.

Thermites are a subset of energetic materials, usually in powder form, made by a metal-metal oxide couple, able to release a noticeable amount of heat upon ignition. The possibility to select formulations that are relatively insensitive to external stimuli and non-toxic is a strong advantage. Moreover, the formulation can be selected and treated to tailor its temperature of ignition, assuring a predictable behaviour. This extra heat source could be placed in the structural voids of the most robust components (e.g. ball bearing units and solar array mechanisms) to promote their demise, acting only where it is needed. In addition, thermite action could be used to provoke a controlled fragmentation in the upper atmosphere, weakening the structural joints of the spacecraft and hence exposing a higher surface area during the re-entry.

The Thermite-for-Demise (T4D) approach has been already partially studied and tested [4–7], but a systematic research involving the rigorous selection of the energetic material, experiments, and their numerical reconstruction is still lacking.

This paper presents a re-entry demise model including the effect of a thermite charge placed on board. The activity aims at supporting the definition of the demise strategies with an additional pyrotechnic heat source in terms of mass, material reactivity, heat release profile, and total enthalpy release. An investigation of the heat transfer principles between a reacting thermite and its containing vessel, subject to an external convective heat source, is used to characterize experimentally the effective heat transfer process.

In Section 3 the experimental set-up for the quantification of the heat transfer efficiency between the thermite charge and its vessel is described. The obtained results are later presented and analyzed in Section 4. In Section 5 the numerical model used for the preliminary sizing of the T4D application is detailed, while in Section 6 the numerical results regarding the predicted spacecraft to thermite mass ratio and the best temperature of ignition are presented. Finally, Section 7 reports the main conclusions of this research and the main considerations that will be taken into account in the next steps of the project.

2. Background

As stated in [3], the main requirement for space debris mitigation in Low Earth Orbits is to deorbit the spacecraft no later than 25 years after the end of its mission, guaranteeing a ground casualty risk lower than 10^{-4} and, if an uncontrolled re-entry is foreseen, a maximum fragment energy of 15 J.

A controlled re-entry can be useful to comply with the 25-years rule and to avoid the issues related to the casualty risk on ground, impacting Earth surface in the South Pacific Ocean Uninhabited Area (SPOUA). A final high-thrust manoeuvre must be performed, as it is needed to enter the atmosphere with a steep angle, limiting the aftermath of uncertainties (e.g., atmosphere properties) on the ground impact point. A controlled re-entry is typically needed for massive spacecrafts (generally having more mass than 2 tons). This implies noticeable impact on spacecraft design and cost. The high-thrust last burn typically necessitates the presence of a dedicated chemical rocket engine on the satellite. This could be particularly impactful for spacecrafts that need just an electrical propulsion system to perform their mission. For satellites that already have a suitable chemical thruster, a significant fraction of propellant must be allocated for the last burn [4]. The extra propellant mass needed on board impacts also on the size of the propellant subsystem itself, leading to an even higher aftermath on the satellite mass and, hence, on the mission budget. Moreover, the increase of complexity in the design and in the mission affects the reliability of the Post Mission Disposal (PMD). European Space Agency (ESA), Japan Aerospace Exploration Agency (JAXA), and National Aeronautics and Space Administration (NASA) have recently signed an agreement on PMD topic, where it is stated that such reliability should be at least of 90% [8].

An uncontrolled re-entry would avoid these drawbacks. Generally, satellites with an orbit lower than 600 km are naturally compliant with the 25-years rule, without a dedicated system or manoeuvre. But even for satellites that spend their operative life at higher altitudes, a controlled re-entry to assure the compliance to this rule may not be necessary. Different passive devices (e.g., drag sails [9] and tethers [10]) are under study to lower the residence time in space, but also a long low-thrust manoeuvre performed with electric thrusters could lower the perigee enough to be compliant to the 25-years rule. Nevertheless, the residence time requirement is not the only one that must be assessed for an uncontrolled re-entry. The limits on the casualty risk and on the maximum energy of the generated fragments must be quantified by re-entry simulations and could prevent an uncontrolled deorbit.

2.1. Re-entry codes

Atmospheric re-entry is a complex process, subject to a high number of uncertainties. A complete re-entry model must be able to simulate the flight dynamics, the aerothermodynamics, the heat transfer processes in the spacecraft itself, the mechanical stresses, and their effects on fragmentation. The solar activity cycle, various unpredictable atmospheric properties, and the random tumbling typically experienced by satellites at re-entry lead to the necessity of a stochastic approach (usually via a Monte Carlo analysis) to foresee the surviving fragments and their footprint on ground. This estimate allows a quantification of the casualty risk and of the maximum fragment energy.

Various models have been proposed to perform this task, at different level of detail. In the European framework, the baseline is represented by the Debris Risk Assessment and Mitigation Analysis (DRAMA) [11], the suite provided by ESA to spacecraft builders to prove their compliance to the debris mitigation requirements. This software falls in the category of object-oriented tools, in which structure and main components of the satellite are modelled as simple shapes (sphere, cylinder, cone and box), initially nested and then released either at certain altitudes or when the external shell reaches its melting temperature. These simple shapes are called primitives, and if they are nested at the same level it is possible to structurally connect them between each other. When a relation of inclusion or connection is broken, as foreseen by the aerothermodynamic model, a fragmentation occurs. The dynamics of the model is given by a 3 Degrees Of Freedom (DOF) set of equations. For the continuum regime, the stagnation heat rate of a sphere is computed using the Detra-Kemp-Riddell correlation. In the free molecular regime, the same quantity is defined as $\dot{q}_{st_{fm}} = \alpha_T \rho_\infty V_\infty^3/2$, where $\dot{q}_{st_{fm}}$ is the stagnation heat rate of the sphere, α_T is an accommodation factor equal to 0.9, ρ_∞ is the freestream density, and V_∞ is the freestream velocity. A bridging function is used between these two values in the transition regime. The stagnation heat rate of a sphere is used to compute the heat received by the other supported primitives, assuming random tumbling and using a set of shape factors. These methodologies are common among the object-oriented codes (e.g., NASA's Object Reentry Survival Analysis Tool, ORSAT) [12].

Despite ESA demands to assess the compatibility to casualty risk and energy requirements through DRAMA suite, it is possible to use more detailed software for this computation [13]. The most prominent example of more detailed model is HTG's Spacecraft Atmospheric Re-entry and Aerothermal Breakup (SCARAB) [14]. SCARAB is a panel-based software that allows the complete modelling of the spacecraft. An arbitrarily complex geometry can be discretized, and the resulting panels are then used to compute the dynamics and thermodynamics of the re-entry. Each element is characterized by its own set of properties (e.g., mass, moment of inertia, temperature). The discretization allows to use the complete set of 6 DOF equation for the trajectory computation and a better representation of the temperature field in the spacecraft. This representation consents to abandon the standard random tumbling assumption and to include heat conduction inside the primitives in the thermal model. The Newtonian theory and the

modified Lees theory are used in the continuum flow, respectively for the aerodynamic and aerothermodynamic models. In the free-molecular flow, Nocilla or Schaaf-Chambre accommodation coefficients are used. This approach, named spacecraft-oriented, is inherently different from the object-oriented one as the needed simplification of the spacecraft is much lower. Other noticeable re-entry models in the European framework are the Spacecraft Aerothermal Model (SAM), which aims to provide a hybrid spacecraft-/object-oriented approach [15], and PAMPERO, a rather recent spacecraft-oriented code developed by CNES [16].

A problem common to all re-entry models is the lack of reliable experimental data for validation. Basic tuning of key parameters can be based on re-entry observations, but significant validation datasets are still not available. The most important example is the Vehicle Atmospheric Survivability Test/Project (VAST/VASP) study [17], which provided the research community a first indication of the main breakup altitude for a real case. An important step in this sense will be the ESA project DRACO (Destructive Re-entry Assessment Container Object), planned to be launched in 2027, that will be the first demonstration of a controlled breakup process to extrapolate data. As for ground tests, important experimental data can be obtained by studying spacecraft components in wind tunnels. These investigations can provide material characteristics (e.g. ESA's ESTIMATE, European Space maTerIal deMisability dATabasE [18]) of paramount importance for a destructive re-entry model, even if limited by the impossibility of testing tumbling objects or representative dynamic heat flux conditions.

2.2. Design for Demise

Design-for-Demise (D4D) is the intentional design of a spacecraft to make it demise during an atmospheric re-entry. This design methodology can be particularly useful for satellites that, according to destructive re-entry codes, are not compliant with the casualty risk limit. If the foreseen casualty risk is close enough to the limit, a controlled re-entry and its economic burden can be avoided by properly applying D4D concepts. If applicable, D4D can lead to a simpler, lighter, cheaper, more sustainable, and more reliable spacecraft. The impacts on the satellite design workflow can be limited by considering D4D in an early phase of the spacecraft definition, and by choosing the strategy in the D4D portfolio that limits the necessity of re-design. The main limitation of this methodology is that it is relatively new, and while many solutions are currently under research, D4D components are not yet the standard.

D4D can be applied on either system level or equipment level. When a system level approach is considered, satellite components are reorganized such that the most robust equipments, harder to demise, are exposed to the heat load sooner in the re-entry process. On equipment level, the most critical components are identified and solutions to aid their demise are provided. Typically, the most robust components are propellant tanks, valves, gyroscopes, reaction wheels, optical payloads, and solar array drive mechanisms [19].

Several different approaches can be identified to apply D4D at equipment level. A first strategy is to minimize the required heat to reach demise. Minimizing the mass of the component or replacing materials are the most effective solutions [20]. In particular, typical robust components are made of steel, titanium, and silica. If possible, using a material with lower heat capacity, melting point, emissivity or enthalpy of fusion can lower the heat load for demising. A typical example is the replacement of titanium for propellant tanks. The indicated materials are aluminium [21] and composites [22], with solutions currently under development even for the VEGA upper stage AVUM [23]. Nevertheless, the benefits of similar concepts are still under study and discussion [24]. A second approach is to optimize the heat transfer to the components. The main solution proposed for this strategy is to provoke an early, controlled fragmentation of the satellite acting on its structural connections. It is expected to reach demise more easily dividing the spacecraft in smaller fragments, both in mass and in radius of curvature. This approach must be evaluated carefully, as more numerous fragments could imply a wider footprint on ground in case of incomplete demise. This is the rationale behind a third strategy, which is named Design-For-Containment. This methodology consists in keeping fragments together, to limit the casualty area and hence the casualty risk [25]. One last strategy to aid satellite demise is to maximize the available heat. A change of the ballistic coefficient could be helpful to increase the total heat received by the spacecraft during re-entry or to reach a higher maximum temperature, and possibly the melting point of some components. Altering the shape of a component could provoke local increases in the heat flux, possibly enough to provoke local melting. Or, if the available heat from the re-entry process is not enough, an extra source of enthalpy on board may be an option. In this respect the method calls for a safe, highly energetic charge to be activated just when it is needed, to provide the last heat contribution to reach the melting of the component. This is the rationale behind the Thermite-For-Demise (T4D) concept.

2.3. Thermites and mechanical activation

Thermites are a subset of energetic materials, usually in powder form, made by the mix of a metal and of a metal oxide. Once initiated, a oxidation-reduction reaction takes place, producing a more stable oxide and the corresponding metal of the starting oxide. This reaction is typically strongly exothermic and potentially yields partially gasified products [26]. The general form of the reaction is presented in Eq. (1):

$$\mathrm{M}^1 + \frac{x_5}{x_3 x_4}\mathrm{M}^2{}_{x_2}\mathrm{O}_{x_3} \rightarrow \frac{1}{x_4}\mathrm{M}^1{}_{x_4}\mathrm{O}_{x_5} + \frac{x_2 x_5}{x_3 x_4}\mathrm{M}^2 + \Delta H \tag{1}$$

where M^1 and $\mathrm{M}^2{}_{x_2}\mathrm{O}_{x_3}$ are respectively the starting metal and metal oxide, $\mathrm{M}^1{}_{x_4}\mathrm{O}_{x_5}$ and M^2 are the final metal oxide and metal, and ΔH is the enthalpy released in the process. The tunability of thermite reactions (e.g., in terms of reactivity, heat of reaction, product gaseous fraction) has granted to this class of pyrotechnics a wide range of applications [27]. As for all energetic materials, the ignition can be provoked by different energy sources: a thermal load, an irradiation, an electrostatic discharge, or a mechanical effect (e.g., impact or friction). The spontaneity of the overall reaction can be preliminarily studied considering the Gibbs free energy balance between the reactants and products. Similarly, an indication on the reaction temperature and on the physical state of the products can be obtained by thermochemistry computations, considering the reaction to take place adiabatically [26].

The characteristics of the reaction can be tailored by acting on a variety of parameters. The choice of the reactant couple is the first parameter to be considered, as it is a key factor for the spontaneity of the reaction and the heat released. Typically, the chosen fuel is aluminium, due to its availability and non-toxicity. The range of properties that can be obtained by different oxidizers is wide, even limiting the fuel choice to Al [28]. Other important factors for the reaction characteristics are the granulometry of the reactants, the oxidizer to fuel ratio, and the compaction. In particular, nanometric-sized thermites show interesting features. Their reduced granulometry implies a higher surface area that, in turn, results in an incremented reactivity and a superior combustion velocity, that can reach an explosive behaviour [29].

A further degree of freedom to alter powder characteristics is given by activation. Activation processes are divided into three families: chemical, mechanical, and mechanochemical. This paper focuses on the purely mechanical activation. In this kind of process, the powder is placed in a vial together with a milling tool (e.g. metallic balls or rods). A process control agent (PCA) can be introduced as well, if needed. The PCA is typically a substance that is introduced to limit some chemical reactions that could take place during the activation process, but which are not desired in the final product. Once closed, the vial is mounted on a mixer that induces the movement of the vial. The powder is then grinded by the collisions of the milling tools between each other and with the walls of the vial. The milling process causes an alteration in

shape, granulometry, and surface finishing of the powder. If different substances in powder form were introduced in the vial, a submicron mixing can be induced and a micro- or nanostructured powder can be obtained. Relevant references about mechanical activation process are [30–32].

Many different parameters can be adjusted to tailor the final characteristics of the product [33]. The type of mixer (shaker, planetary or attritor), the vial and milling tools shape and material, the ball-to-powder ratio, the PCA substance and its quantity, the milling time and the milling speed are the main parameters that can be varied to control the changes induced to the powder. Considering energetic materials, and thermites in particular, the main characteristics that can be controlled are the reactivity and the combustion speed. The features of the final product are in between the ones of the standard micrometric powder and of the nanometric one, but preserving the micrometric granulometry. The possibility of tailoring the temperature of ignition of the thermite, as well as the beneficial safety features due to the micrometric granulometry, are of paramount importance for a space application, as T4D.

Another relevant topic for a T4D application is thermite ageing. The use of a pyrotechnic charge at the end-of-life of a spacecraft implies significant storage time, both on ground (months up to one year) and on board (decades, considering the 25-year-time-span conceded by the international guidelines for deorbiting). Literature on ageing properties of thermites is limited, and systematic studies are not available. Considering aluminium-based thermites, research on aluminium powder ageing can provide important information. Paravan et al. [34] showed the effect of moisture depending on granulometry. Nano-sized Al (40 nm) powder proved to be particularly sensitive to storage time in high-humidity environment (relative humidity equal to 80%), losing almost all the active metal content in just one day. On the contrary, a coarser powder (30 μm) lost only 13% of the active metal content in 336 h storage time in the same conditions. Few thermite compositions have been studied from the ageing point of view. Among these, Al+CuO composition in both nanopowder [35] and nanolaminate [36] forms was investigated. After 13 months, only limited impact on thermite performances was reported for nanopowders. As for nanolaminates, storage up to 30 years at ambient conditions seems not to affect combustion properties. On the contrary, annealing at 200 °C can lead to a drop in energy reservoir up to 40% in 14 days. The bilayer thickness has a paramount importance in this process, as if a thicker bilayer is considered (1 μm) the drop in energy reservoir falls to the 6%. Another thermite mixture that was studied is Al+Fe_3O_4 [37]. In this case the powder was hot pressed into pellets at 425 °C for 7 min. A growth in the oxide layer thickness was observed, from 0.99 nm up to 3.1 nm. After this process, no significant effects were detected after ageing at 180 °C in open air. Summarizing, thermite ageing remains an open topic. Even if thermites can be considered rather stable, moisture is probably the most consistent threat for these formulations. A coarser granulometry seems to be beneficial, limiting the ageing effects.

2.4. Heat transfer

One of the main preparatory tasks for the design of a T4D application is to determine the fraction of heat that can be expected to be transferred by the ignited thermite to the surrounding vessel. This value, that will be called heat transfer efficiency η in the following, is a key parameter for a correct sizing of the charge to place on board.

Thermites are commonly used to cut, destroy, or simply transfer heat to a target. Nevertheless, the quantification of the fraction of the theoretically available heat effectively transferred to the target is still not clear. Many terrestrial applications involve the expulsion of the reacted material through a nozzle, creating a jet that impinges on a substrate to provoke a hole or a cut (e.g., [38]). This kind of application is commonly referred to as a “thermal torch” and mainly relies on the convective heat transfer between the jet and the target. Gas generation, distance between nozzle and target, and the characteristics of the ejected particles are the main driving parameters for these applications. Crane et al. [39] analyzed a silicon substrate previously exposed to a jet given by the reaction of thermites of different granulometries. The results indicated higher performance of the micrometric thermite with respect to the nanometric one, and this outcome was attributed to the higher kinetic energy of the bigger particles. In a similar study, Collins et al. [40] highlighted the importance of the heat capacity and density of the impinging particles. While a T4D application mainly relying on convective effects can be conceived, the focus of this paper is on a conductive heat transfer process. In this last concept, the thermite is placed inside a cavity of the target and transfers heat in direct contact with the object. For such a conductive concept, literature on the topic is rather poor. Crane et al. [41] studied the energy transfer from a reacting thermite to a v-notch shaped steel substrate, quantifying the efficiency to 10%. The high losses registered were attributed to convection, radiation, and gas production. In a T4D application it is evident that the geometry needs to be confined and this aspect could influence deeply the heat transfer efficiency. Once the expected heat transfer efficiency is determined, it would be possible to preliminarily size a space application, investigating key parameters as the ratio between spacecraft and thermite mass or the best ignition temperature of the energetic material to be used.

An important topic that will need to be investigated in detail in further research is the position of the thermite charge on the spacecraft. Its position influences the maximum temperature reached during the re-entry process, the heating rate, and the heat transfer to the surrounding elements. If the thermite is placed nearby the external profile of the spacecraft, the loss of unreacted material could limit the efficiency of the technique. If the charge is placed more internally, a suitable formulation should be chosen to assure ignition at lower temperature. In this paper, only simple geometries (hollow sphere, cylinder, and box) will be investigated, considering the thermite vessel directly exposed to the flow during re-entry.

3. Experimental set-up and materials

3.1. Experimental set-up

The objective of the hereby presented set of experiments was to quantify, in non-relevant environment, the heat transfer between a thermite charge and the vessel in which it is contained. The selected vessel was an AISI 316L tube, filleted at the ends. Its length was 100 mm, its external diameter 12.7 mm and its internal diameter 9.1 mm. Both the ends of the tube were closed by an AISI 316L hexagonal cap. The geometry was then heated by using a hot air blower (Leister Hotwind “S”), to provoke the ignition through an external convective heat source. Given the limited maximum temperature reachable by the hot air source (around 900 °C), the use of an activated thermite powder was necessary. The blower was used at its maximum temperature in each ignition test. The hot air flow characterization is reported in Appendix A. The lower cap, that contained the thermite, was placed in correspondence of the axis of the blower section, at 0.5 cm from it. This setting was necessary to maximize the heat transfer to the vessel and assure powder ignition. The thermal evolution of the vessel was recorded using a set of N-thermocouples, which diameter was 0.75 mm. For each component (tube and two caps) a thermocouple was placed on its external surface, at the half of its height. A thin layer of Boron Nitride paste was used to promote the heat transfer between the thermocouple end and its metallic substrate, with the additional function of maintaining the thermocouple in position during the whole test. The data logger sampled the temperature every 300 ms. The scheme of the experimental set-up is shown in Fig. 1.

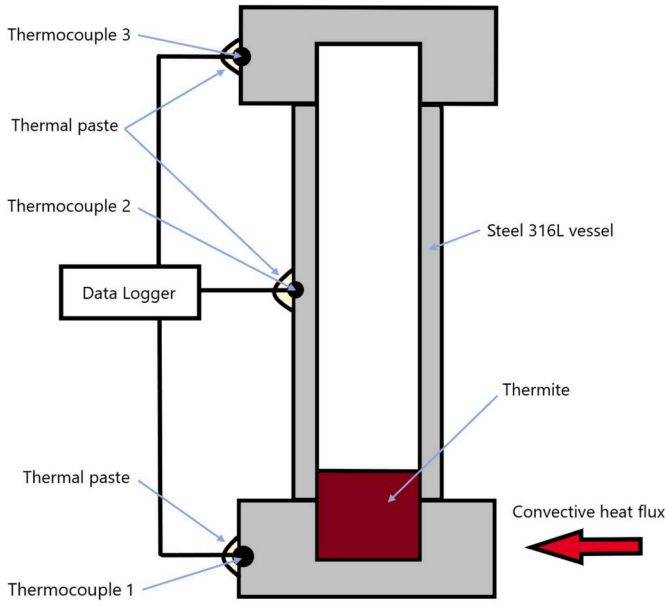

Fig. 1. Scheme of the experimental set-up for the ignition tests.

Table 1
Thermite ($Al+Fe_2O_3$) formulations used in the experiments. The standard micrometric powder is indicated by μ, while the mechanically activated one by μAct. Possible configurations are loose (L) and pelletized (P).

Identifier	Weight [g]	Type	Configuration
1	1	μ	L
	0.5	μAct	L
2	0.66	μ	L
	0.44	μAct	L
3	1	μ	L
	0.5	μAct	L
4	1	μ	L
	0.6	μAct	P
5	1	μ	L
	0.6	μAct	P
6	2.3	μ	L
	0.6	μAct	P

3.2. Materials

The selected thermite, supplied by ReActive - Powder Technology S.R.L., was a stoichiometric mixture of Aluminum and Iron (III) Oxide (Fe_2O_3), that reacts as per Eq. (2) with a theoretical enthalpy release ΔH of 945.4 cal/g (or 3958.20 kJ/kg) [26].

$$2Al + Fe_2O_3 \rightarrow Al_2O_3 + 2Fe + \Delta H \tag{2}$$

The thermite powder was tested in both loose (L) and pelletized (P) form. Moreover, two different types of powder have been evaluated: standard micrometric (μ) and mechanically activated (μAct) thermite. The formulations used in the tests are detailed in Table 1.

4. Experimental results

The output of the experimental setup presented in Section 3 is the thermal history of the steel vessel, that must be properly processed to determine the heat transfer efficiency. An example of the registered temperature profiles can be seen in Fig. 2. To highlight the expected profile behaviour in absence of thermite ignition but considering the thermal inertia of the system, including the charge, a baseline curve is defined. The baseline curve is generated through a numerical fit between the thermite ignition temperature and the asymptotical temperature value of each component.

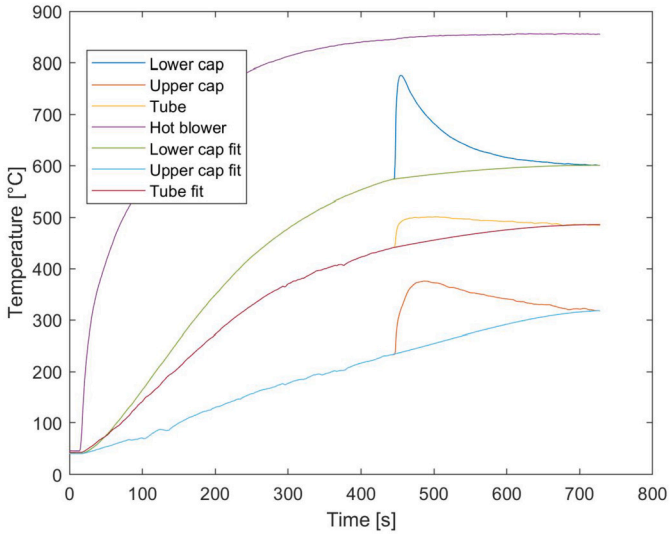

Fig. 2. Example of experimental temperature profiles and numerical fits (Test 6).

For each test, the heat transfer efficiency η has been computed as follows:

$$\eta = \frac{Q_{l,c} + Q_t + Q_{u,c}}{Q_{th}} \tag{3}$$

where $Q_{l,c}$, Q_t and $Q_{u,c}$ are respectively the heat received by the lower cap, the tube and the upper cap, while Q_{th} is the theoretical heat release of the thermite, defined as:

$$Q_{th} = m_{th} Q_{react} \tag{4}$$

in which m_{th} is the thermite mass, reported in Table 1 and Q_{react} is the theoretical heat release for unit mass.

The received heat by each component has been computed taking into account the temperature jump between the ignition and the maximum temperature reached during the test. Indicating with x the generic component, the received heat has been computed through the following equation:

$$Q_x = m_x c_p (T_{max,x} - T_{fit,x}) \tag{5}$$

where m_x is the mass of the component itself and c_p is its specific heat. Note that the estimated Biot number for each object in the direction of the air flow is in the order of 0.01 - 0.05, therefore it is hereby assumed that the temperature is uniform in each body. Even if the tube temperature is not constant in its longitudinal direction, for this computation it was assumed as uniform and equal to the value measured by the thermocouple. The value considered for c_p in the computation is the average between the values reported in [42] for $T_{max,x}$ and $T_{fit,x}$. The temperature $T_{max,x}$ is the temperature of the component at the same instant in which the lower cap reaches its maximum value. In similar way, the temperature $T_{fit,x}$ is the one of the component, predicted by the baseline curve, at the same instant of time. It is preferred to use this value because it takes into account the convective heat provided by the hot air blower during the thermite burning time. In this way, it is possible to estimate the heat transfer efficiency η for each test. The computed values are shown in Table 2. It should be noted that the heat losses due to convection and radiation from the vessel to the environment have been neglected. The different temperature increase rate that can be observed in Fig. 2 indicates that the setup is not in equilibrium and that thermal losses are experienced. This is the topic of a study

Table 2
Heat transfer efficiency values registered in the performed tests.

Identifier	Heat transfer effectiveness, η
1	0.50
2	0.74
3	0.63
4	0.56
5	0.66
6	0.50
Mean	0.60
Standard deviation	0.09

currently ongoing at the Space Propulsion Laboratory of Politecnico di Milano. Nevertheless, this means that the hereby presented values are underestimating the thermite heat transfer to the vessel and, hence, the outcomes are conservative.

The obtained values show a significant variance, spanning from 0.5 to 0.75. In any case, the heat transfer efficiency is noticeably higher than the one obtained in the study by Crane et al. [41]. The main difference with respect to the cited research is the geometry of the vessel. In the hereby presented experiment, the thermite is completely confined inside a vessel, eliminating convective and radiative losses in the energy transfer between the thermite charge and its vessel. The mean value, shown again in Table 2, has been then used in the re-entry code, for a preliminary sizing of the thermite charge for a T4D application.

5. Numerical model

In order to support the preliminary studies for a real T4D application, a Python numerical model named TRANSIT (TRANsatmosferic SImulation Tool) has been developed. TRANSIT is an object-oriented tool which scope is to provide a simple and fast numerical support for the evaluation of thermite application in the re-entry phase. In this section, the numerical scheme for the 0D approach will be presented, while in Section 6 the numerical results regarding the preliminary sizing will be shown. If interested in similar numerical models, the reader can refer to the works of Trisolini [20] and of Rafano Carná and Bevilacqua [43].

5.1. Atmospheric and gravitational model

The atmospheric model chosen for TRANSIT is the NRL-MSISE-00 [44]. The most important advantage of this model is the capability of retrieving the molar densities of the main species composing the atmosphere at a given altitude, longitude and latitude. This particular feature of the model will be used later to compute hot air dissociation after the shock wave.

As for the gravitational model, the non-spherical shape of the Earth is considered up to the fourth degree through a zonal harmonic description. The radial and the tangential components of gravitational acceleration (indicated respectively as g_r and g_t) are described by the following equations [45]:

$$g_r = \frac{\mu}{r^2}\left[1 - \frac{3}{2}J_2(3\cos^2\Phi - 1)\left(\frac{R}{r}\right)^2 - 2J_3\left(\frac{R}{r}\right)^3(5\cos^3\Phi - 3\cos\Phi) - \frac{5}{8}J_4\left(\frac{R}{r}\right)^4(35\cos^4\Phi - 30\cos^2\Phi + 3)\right] \quad (6)$$

$$g_t = -\frac{3\mu}{r^2}\left(\frac{R}{r}\right)^2\sin\Phi\cos\Phi\left[J_2 + \frac{1}{2}J_3\frac{R}{r}\sec\Phi(5\cos^2\Phi - 1) + \frac{5}{6}J_4\left(\frac{R}{r}\right)^2(7\cos^2\Phi - 1)\right] \quad (7)$$

where μ is the gravitational parameter of the Earth, r the distance between the re-entering object and the centre of the Earth, Φ the colatitude, R the radius of the Earth and $J_1, ..., J_4$ the Jeffery constants up to the fourth degree.

5.2. Dynamic model

The selected model [45] to represent the ballistic re-entry considers three degrees of freedom and is expressed in a frame rotating with the atmosphere. Lift is neglected as usually satellites or rocket bodies have no particular aerodynamic shape. Moreover, as the purpose of a T4D application is to be used in uncontrolled re-entries, no thrust is considered. The trajectory of the re-entry, under these assumptions, can be obtained with the following set of ordinary differential equations (ODEs):

$$\dot{r} = \sin\phi \quad (8)$$

$$\dot{\chi} = \frac{v}{r}\cos\phi\cos A \quad (9)$$

$$\dot{\psi} = \frac{v\cos\phi\sin A}{r\cos\chi} \quad (10)$$

$$\dot{v} = -\frac{D}{m} - g_r\sin\phi + g_t\cos\phi\cos A - \omega^2 r\cos\chi(\cos\phi\cos A\sin\chi - \sin\phi\cos\chi) \quad (11)$$

$$\dot{A} = \frac{v}{r}\cos\phi\sin A\tan\chi - \frac{g_t\sin A}{v\cos\phi} + \frac{\omega^2 r\sin A\sin\chi\cos\chi}{v\cos\phi} - 2\omega(\tan\phi\cos A\cos\chi - \sin\chi) \quad (12)$$

$$\dot{\phi} = \frac{v}{r}\cos\phi - \frac{g_r\cos\phi}{v} - \frac{g_t\sin\phi\cos A}{v} + \frac{\omega^2 r\cos\chi}{v}(\sin\phi\cos A\sin\chi + \cos\phi\cos\chi) + 2\omega\sin A\cos\chi \quad (13)$$

In which v is the relative velocity of the re-entering object with respect to the atmosphere, ϕ the flight path angle, χ the latitude, ψ the longitude, A the heading angle, D the drag force, m the spacecraft mass and ω the angular rotational velocity of the Earth.

5.3. Aerodynamic model

Given the very different conditions in terms of density, pressure and temperature that an object re-entering the atmosphere has to face, it is common to divide the re-entry process in three regimes [46]:

1. Free molecular regime, for $Kn \geq 10$;
2. Transitional regime, for $0.01 < Kn < 10$;
3. Continuum regime, for $Kn \leq 0.01$.

The classification into the three regimes is based on the value of the Knudsen number (Kn), that can be defined as follows:

$$Kn = \frac{\lambda}{L_c} \quad (14)$$

where λ is the mean free path between successive collisions of air molecules and L_c is the characteristic length of the considered geometry. The classification of the different regimes is of paramount importance to select the correlations to determine the drag coefficient, C_D, and the convective heat flux experienced by the spacecraft, $\dot{q}_{conv}$. As for the former one, the selected correlations for the three geometries considered in this model are shown in Table 3 and taken from [20]. These correlations were obtained through experiments in hypersonic wind tunnels or theoretical analyses. The original sources are reported in Table 3.

In Table 3, l_c is the cylinder length, r_c the cylinder radius, A_x, A_y and A_z are the surfaces defined by the three box's dimensions L, H and

Table 3
Selected correlations for the drag coefficient, for the three different geometries and regimes.

Geometry	Free molecular	Transitional	Continuum	Reference
Sphere	2	Bridging function	0.92	[47]
Cylinder	$1.57 + 0.785\left(\frac{l_c}{2r_c}\right)$	Bridging function	$0.7918 + 0.326\left(\frac{l_c}{2r_c}\right)$	[48]
Box	$1.03\left(\frac{A_x+A_y+A_z}{median(A_x,A_y,A_z)}\right)$	Bridging function	$0.46\left(\frac{A_x+A_y+A_z}{median(A_x,A_y,A_z)}\right)$	[49]

W. The bridging function used for the transitional regimes is the same for all the geometries:

$$C_D^{TR} = C_D^C + (C_D^{FM} - C_D^C)\sin^2\xi \tag{15}$$

where C_D^{TR}, C_D^C and C_D^{FM} are the values of the drag coefficient respectively in the transitional, continuum and free molecular regimes. The variable ξ is defined as follows:

$$\xi = \pi(a_1 + a_2 \log_{10} Kn) \tag{16}$$

In which:

$$a_1 = -\frac{1}{2}\left(\frac{\log_{10} Kn^{CR}}{\log_{10} Kn^{FM} - \log_{10} Kn^{CR}}\right) \tag{17}$$

$$a_2 = \frac{1}{2}\left(\frac{1}{\log_{10} Kn^{FM} - \log_{10} Kn^{CR}}\right) \tag{18}$$

where Kn^{FM} and Kn^{CR} are the previously mentioned boundaries for defining the different regimes, respectively equal to 10 and 0.01.

5.4. Aerothermodynamic model

The final outcome of the aerothermodynamic model is to provide the heat load experienced by the spacecraft during the re-entry, that is mainly function of the geometry of the spacecraft itself and of the flow regime. The following subsections present the strategy and correlations used to obtain the heat load for the three geometries considered (sphere, cylinder and box) in the different flow conditions previously presented.

5.4.1. Shape factors

As the most common heat correlations for hypersonic re-entry refer to a constant-attitude sphere or plate on its stagnation point, shape factors can relate this value to the appropriate one for the geometry under consideration, during a random tumbling re-entry. Given the 0D approach that has been chosen for this work, the distinction between the three geometries is then obtained following this strategy. The shape factor values will be later multiplied by the convective heat flux, representing the tumbling motion of the selected geometry. The main source for these values is again [20].

The sphere is simply characterized by two constant shape factor values, one for the free molecular regimes, F_{sph}^{FM}, and one for the continuum regime, F_{sph}^{C}.

$$F_{sph}^{FM} = 0.255 \tag{19}$$

$$F_{sph}^{C} = 0.217 \tag{20}$$

These values are derived from theoretical considerations presented by Klett [48] for a disk, in case of free-molecular regime, and from the value used in SAM and discussed in [20] with respect to other literature theoretical results, in case of continuum regime.

As for the cylinder geometry in free molecular regime, the following equation is used:

$$F_{cyl}^{FM} = \frac{2F_{end}^{FM}A_{end} + F_{side}^{FM}A_{side}}{A_{tot}} \tag{21}$$

where F_{cyl}^{FM} is the cylinder shape factor in free molecular regime, A_{end} its base surface, A_{side} its lateral surface and A_{tot} its total external surface. The other two terms, F_{end}^{FM} and F_{side}^{FM}, are defined as:

$$F_{end}^{FM} = 0.255 \tag{22}$$

$$F_{side}^{FM} = 0.785 \cdot Y + 0.5 \cdot Z \tag{23}$$

The curve Y represents the ratio of average heating on the sides of a rotating, side-on cylinder to heating to surfaces perpendicular to the flow, in free molecular conditions. The function Z, instead, represents the ratio of heating on surfaces parallel to flow to heating on surfaces perpendicular to flow, again in free molecular conditions. Both the curves were described by Klett in [48]. Regarding the continuum regime, Eq. (21) is still used but with proper change in F_{end}^{C} and F_{side}^{C}:

$$F_{end}^{C} = 0.323 \tag{24}$$

$$F_{side}^{C} = 0.179 + 0.333 \cdot B \tag{25}$$

where the curve B represents the ratio of average heating to the side of an end-on cylinder to stagnation point heating to a sphere of the same radius. Again, [48] is the source of this approach.

The box geometry is converted to an equivalent cylinder and then Eq. (21) is applied. Given the three dimensions of the box, L, H and W, with $L \geq H \geq W$, the equivalent cylinder length l_c and radius r_c are computed as follows:

$$l_c = L \tag{26}$$

$$r_c = \frac{\sqrt{H+W}}{2} \tag{27}$$

This approach resembles the one proposed in [49], but the radius is halved as, with this modification, the final results are in greater accordance with a significant set of commercial re-entry software (SCARAB and SAM, see Section 5.7).

5.4.2. Free molecular regime

The reference heat used in this model for the free molecular regime is the heat load registered by [48] for a plate perpendicular to the flow:

$$\dot{q}_{ref}^{FM} = 11356.6 \cdot \frac{a_{ref}\rho_1 v_1^3}{1156} \tag{28}$$

in which a_{ref} is an accommodation coefficient, here considered constant and equal to 0.9, ρ_1 is the free-stream density and v_1 is the free-stream velocity. This reference heat is then multiplied for the appropriate shape factor F^{FM} to obtain the convective heat flux $\dot{q}_{conv}$. So, for the free molecular regime:

$$\dot{q}_{conv}^{FM} = F^{FM}\dot{q}_{ref}^{FM} \tag{29}$$

5.4.3. Continuum regime

In the continuum regime, the formation of a shock wave in front of the spacecraft provokes a sudden increase of temperature that in turn leads to dissociation of the molecules in the air flow. Given the importance of this phenomenon on the heat load experienced by a spacecraft during re-entry, a model for the complete characterization of the flow field was adopted [43]. As the final outcome of the thermochemical module is to provide the reference value for the heat load to be multiplied for the shape factor, and because the hereby considered reference value is the stagnation heat flux on a sphere, the shock wave can be considered normal without checking if it should be attached or not. The hot air after the shock will be considered as a non-calorically perfect gas in chemical equilibrium.

The main inputs of the numerical scheme are the atmospheric pressure p_0, density ρ_0 and incoming flow velocity v_0, all for free-stream conditions. Tannehill and Mugge [50] provide curve fits for the computation of hot air properties that allow the computation of the enthalpy h, the temperature T and the entropy s from the values of pressure p, density ρ and internal energy e:

$$h = h(p, \rho) \tag{30}$$

$$T = T(p, \rho) \tag{31}$$

$$s = s(e, \rho) \tag{32}$$

Using Eq. (30), the free-stream enthalpy h_1 is obtained as follows:

$$h_1 = h(p_1, \rho_1) \tag{33}$$

It is now possible to compute the properties of the air flow after the bow shock, following the algorithm proposed by Anderson [46]. These properties will be later indicated by the subscript 2. This fixed-point algorithm starts guessing the value of the ratio ρ_1/ρ_2, that the author suggests considering at the first iteration equal to 0.1. It is then possible to compute the pressure p_2 and the enthalpy h_2 with the Eq. (34) and (35).

$$p_2 = p_1 + \rho_1 v_1^2 \left(1 - \frac{\rho_1}{\rho_2}\right) \tag{34}$$

$$h_2 = h_1 + \frac{v_1^2}{2}\left[1 - \left(\frac{\rho_1}{\rho_2}\right)^2\right] \tag{35}$$

Eq. (30) can be inverted and solved by a non-linear solver to compute ρ_2:

$$\rho_2 = \rho(p_2, h_2) \tag{36}$$

Now ρ_1/ρ_2 can be computed again, as well as the error with respect to its previous value. Until this error does not reach an acceptable value, the procedure is iterated. The other properties across the shock can be computed in a straightforward manner:

$$v_2 = v_1 \frac{\rho_1}{\rho_2} \tag{37}$$

$$T_2 = T(p_2, \rho_2) \tag{38}$$

$$e_2 = h_2 - \frac{p_2}{\rho_2} \tag{39}$$

The conditions at the stagnation point, indicated with the subscript $t,2$, can be now computed. The enthalpy at the stagnation point can be obtained as follows:

$$h_{t,2} = h_1 + \frac{1}{2}v_1^2 = h_2 + \frac{1}{2}v_2^2 \tag{40}$$

As the transformation is isoentropic, $s_2 = s_{t,2}$. The numerical fits can be used again to compute $p_{t,2}$, $\rho_{t,2}$ and $e_{t,2}$ solving the following set of non-linear equations:

$$e_{t,2} = h_{t,2} + \frac{p_{t,2}}{\rho_{t,2}} \tag{41}$$

$$s_{t,2} = s(e_{t,2}, \rho_{t,2}) \tag{42}$$

$$h_{t,2} = h(p_{t,2}, \rho_{t,2}) \tag{43}$$

Once the non-linear set is solved, the temperature at the stagnation point can be obtained as $T_{t,2} = T(p_{t,2}, \rho_{t,2})$. The dynamic viscosity can now be computed using Sutherland's law:

$$\mu_{t,2} = 1.458 \cdot 10^{-6} \cdot \frac{k_D T_{t,2}^{1.5}}{T_{t,2} + 110.4} \tag{44}$$

where the introduction of the coefficient $k_D = 1.1$ accounts for the high temperature at the edge of the boundary layer. Considering constant the pressure across the thin boundary layer, $p_{t2} = p_w$, it is possible to start computing the properties at the wall, here indicated with the subscript w. The density at the wall ρ_w can be obtained inverting Eq. (31):

$$\rho_w = \rho(p_w, T_w) \tag{45}$$

while the enthalpy at the wall can then be computed using Eq. (30):

$$h_w = h(p_w, \rho_w) \tag{46}$$

The dynamic viscosity at the wall, μ_w, can be obtained again through Sutherland's law:

$$\mu_w = 1.458 \cdot 10^{-6} \cdot \frac{T_w^{1.5}}{T_w + 110.4} \tag{47}$$

The last useful flow property that will be later used for the computation of the convective stagnation heat flux is the Prandtl number at the wall, Pr_w, defined as:

$$Pr_w = \frac{c_{p,w}\mu_w}{k_w} \tag{48}$$

where $c_{p,w}$ and k_w are respectively the specific heat capacity and the conductivity of air at temperature T_w.

It is now possible to compute the chemical composition of the flow behind the shock wave using the temperature $T_{t,2}$ and the pressure $p_{t,2}$. The densities of the species composing the air before the shock wave are given by the NRL-MSISE-00 atmospheric model, depending on the latitude, longitude and altitude of the spacecraft. Five different species are considered in this model: O, O_2, N, N_2 and NO. The numerical scheme for an equilibrium chemically reacting mixture described by Anderson [46] and De Luca [51] is used. In the following, considering the species i, the symbol n_i indicates its molar density (the unknown) and N_i its initially available gram-atom number density (the input from the atmospheric model). As the number of atoms in the considered volume does not change in the dissociation process, it is possible to write the following conservation equations:

$$n_O + 2n_{O_2} + n_{NO} = N_O + N_{O_2} \tag{49}$$

$$n_N + 2n_{N_2} + n_{NO} = N_N + N_{N_2} \tag{50}$$

The thermochemical equilibrium relations give the additional equations to compute the molar densities n_i:

$$\frac{1}{2}\mathrm{O_2} \leftrightarrow \mathrm{O}: \quad \frac{n_O}{\sqrt{n_{O_2}}} = \sqrt{\frac{n_{tot}}{P}} K_{p,1}(T) \tag{51}$$

$$\frac{1}{2}\mathrm{N_2} \leftrightarrow \mathrm{N}: \quad \frac{n_N}{\sqrt{n_{N_2}}} = \sqrt{\frac{n_{tot}}{P}} K_{p,2}(T) \tag{52}$$

$$\frac{1}{2}\mathrm{N_2} + \frac{1}{2}\mathrm{O_2} \leftrightarrow \mathrm{NO}: \quad \frac{n_{NO}}{\sqrt{n_{O_2} n_{N_2}}} = K_{p,3}(T) \tag{53}$$

where $K_p(T)$ are the specific equilibrium constants for each reaction considered, and can be found in literature (e.g., NIST-JANAF Tables [52]). In Eq. (51), (52) and (53) the unknown n_{tot} is introduced, that is simply defined in Eq. (54) as the total number of moles in the unit volume:

$$n_{tot} = n_O + n_{O_2} + n_N + n_{N_2} + n_{NO} \tag{54}$$

The set of equations is now closed, involving 6 unknowns (n_O, n_{O_2}, n_N, n_{N_2}, n_{NO} and n_{tot}) and 6 equations. A fixed-point iterative approach has been used to compute the solution, using an initial guess for n_{tot} equal to 1.1, as suggested by [51]. Once this set of equations is solved, the composition can be expressed also in terms of molar fractions X_i and the average molar mass M can be computed as of Eq. (55) and (56), respectively.

$$X_i = \frac{n_i}{n_{tot}} \tag{55}$$

$$M = \sum_{i=1}^{5} X_i M_i \tag{56}$$

where M_i is the molecular mass of each species considered. It is now possible to express the chemical formulation in terms of mass fractions c_i:

$$c_i = X_i \frac{M_i}{M} \tag{57}$$

that can be used to obtain the heat of dissociation h_D [53]:

$$h_D = \sum_{i=1}^{5} c_i (\Delta h_f)_i^0 \tag{58}$$

where $(\Delta h_f)_i^0$ is the standard heat of formation of the species i, that can be found again in [52]. The Fay and Riddell [53] correlation can now be used to compute the convective stagnation heat flux $\dot{q}_{ref}^C$ for a spherical geometry in a hypersonic flow in the continuum regime:

$$\dot{q}_{ref}^C = \frac{0.763}{Pr_w^{0.6}} (\rho_{t,2}\mu_{t,2})^{0.4} (\rho_w \mu_w)^{0.1} \sqrt{\left(\frac{\mathrm{d}u_e}{\mathrm{d}x}\right)_{t,2}} (h_{t,2} - h_w) \times \left[1 + (Le^{0.52} - 1)\frac{h_D}{h_{t,2}}\right] \tag{59}$$

in which the Lewis number Le is taken equal to 1.4 as suggested by [53], while the term $\mathrm{d}u_e/\mathrm{d}x$ is the velocity gradient at the stagnation point. This can be approximated as follows, considering inviscid flow:

$$\left(\frac{\mathrm{d}u_e}{\mathrm{d}x}\right)_{t,2} = \frac{1}{R_{eff}} \sqrt{\frac{2(p_{t,2} - p_1)}{\rho_{t,2}}} \tag{60}$$

where R_{eff} is the radius of the blunt body under consideration. For the spherical and the cylindrical geometries the radius is directly employed, while for the box the equivalent cylinder radius is used, defined as shown by Eq. (27).

The reference heat flux is then multiplied by the appropriate shape factor F^C to obtain the value of the convective heat flux in the continuum regime:

$$\dot{q}_{conv}^C = F^C \dot{q}_{ref}^C \tag{61}$$

5.4.4. Transitional regime

For the computation of the transitional regime reference stagnation heat flux $\dot{q}_{ref}^{TR}$, a bridging function between the free-molecular regime value $\dot{q}_{ref}^{FM}$ and the continuum regime one $\dot{q}_{ref}^C$ is used. The selected approach is the one presented in [54] and reported in Eq. (62).

$$\dot{q}_{conv}^{TR} = \frac{\dot{q}_{conv}^C}{\sqrt{1 + \left(\frac{\dot{q}_{conv}^C}{\dot{q}_{conv}^{FM}}\right)^2}} \tag{62}$$

5.4.5. Radiative contribution

The radiative contribution is then added to the convective heat flux. After computing $\dot{q}_{conv}$ according to the flow regime and spacecraft geometry, it is possible to obtain the average heat flux experienced by the spacecraft surface, named $\dot{q}_{NoTh}$ to highlight that this term considers all the terms of the heat load, except for the thermite charge contribution:

$$\dot{q}_{NoTh} = \dot{q}_{conv} - \epsilon k_B T_w^4 \tag{63}$$

where ϵ is the emissivity of the spacecraft material and k_B is the Boltzmann constant ($1.380649 \cdot 10^{-23}$ J/K).

5.5. Thermite model

The last heat flux component that must be considered for a T4D application is the one given by the thermite upon ignition. The reactants are characterized by a theoretically available heat of reaction, Q_{th}, defined by Eq. (4). The mass of the thermite charge m_{th} can be defined with respect to the available volume inside the hollow geometry (Eq. (64)):

$$m_{th} = fill \cdot \rho_{th} V_{int} \tag{64}$$

where $fill$ is the filling factor, spanning from 0 to 1, ρ_{th} is the density of the thermite and V_{int} is the internal volume of the spacecraft. As it has been shown in Section 4, not all the theoretically available heat of reaction is transferred by the ignited thermite to its vessel. The effective thermite heat transferred to the spacecraft during the whole simulation, Q_{eff}, is then represented by Eq. (65).

$$Q_{eff} = \eta \cdot m_{th} Q_{react} \tag{65}$$

The thermite charge will start to release its heat of reaction once the temperature of the wall T_w reaches its ignition temperature T_{ign}, for a certain timespan t_{th}. To account for this, the value of T_w is checked at each timestep and, if greater than T_{ign}, the release of the heat Q_{eff} is started. The heat release proceeds following one of the five possible profiles that can be chosen in TRANSIT:

1. Constant, step-like profile;
2. Gaussian profile;
3. Triangular profile, with maximum heat release at the start of the timespan t_{th};
4. Triangular profile, with maximum heat release at the end of the timespan t_{th};
5. Triangular profile, with maximum heat release at the half of the timespan t_{th}.

The five possible profiles for thermite heat release are shown in Fig. 3. While the mathematical definitions of the constant and triangular profiles are trivial, the Gaussian one implies the choice of two parameters. This heat release profile aims to simulate what could be obtained with a very fast thermite reaction, similarly to an impulsive release of heat. The Gaussian profile is obtained using an expected value μ_G and a standard deviation σ_G described as follows:

$$\mu_G = \frac{t_{th}}{2} \tag{66}$$

$$\sigma_G = \frac{\mu_G}{10} \tag{67}$$

meaning that more than the 95% of the release heat, only for the Gaussian profile, is released in one twentieth of the burning time t_{th}.

As the integral of all the profiles over the timespan t_{th} is 1, the total heat released will be equal to Q_{eff} if the heat flux $\dot{q}_{Th}$ is computed as:

$$\dot{q}_{Th} = \begin{cases} \frac{Q_{eff} P(t-t_0)}{S_{int}} & \text{if } 0 < t - t_0 < t_{th} \\ 0 & \text{otherwise} \end{cases} \tag{68}$$

where $P(t)$ is the normalized heat release profile chosen among the ones shown in Fig. 3 and t_0 is the time value at which $T_w > T_{ign}$ for the first time. Its unit of measure is 1/s.

5.6. Thermal and ablation model

The set of ODEs presented at the beginning of this Section (Eq. (8) - (12)) referring to the kinematic and dynamic variables, must be completed with two additional ODEs to describe the thermal and ablative behaviour of the spacecraft.

Firstly, the contributions from the environment and from the thermite are combined to give the final heat load incoming into the spacecraft, $\dot{Q}_{tot}$:

$$\dot{Q}_{tot} = \dot{q}_{NoTh} S_{ext} + \dot{q}_{Th} S_{int} \tag{69}$$

in which S_{ext} is the external surface, that is computed at each timestep as depends on the initial geometry and on the instantaneous value of the

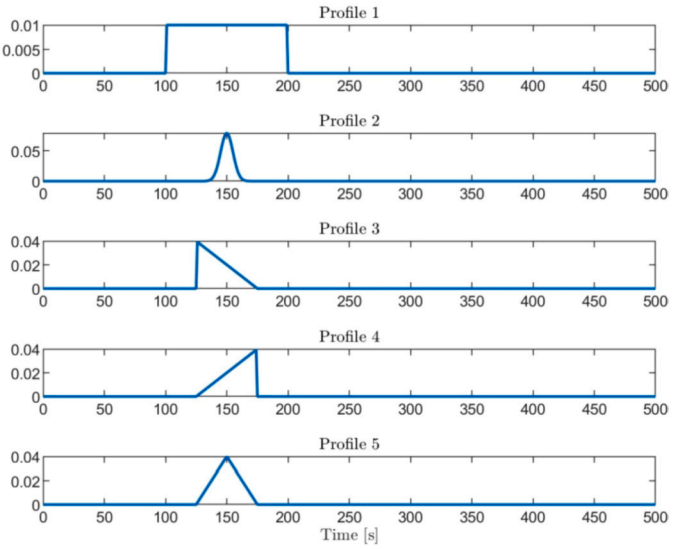

Fig. 3. Heat release profiles adopted in the re-entry model. The duration of the heat release is one of the inputs of the model.

thickness δ. It is now possible to compute the wall temperature from the following ODE:

$$\dot{T}_w = \begin{cases} \frac{\dot{Q}_{tot}}{m_{tot} c_{p,av}} & \text{if } (T_w < T_{melt} \wedge \dot{Q}_{tot} > 0) \vee \dot{Q}_{tot} < 0 \\ 0 & \text{otherwise} \end{cases} \tag{70}$$

where T_{melt} is the melting temperature of the material composing the spacecraft, while the total mass m_{tot} and the average specific heat $c_{p,av}$ are defined by Eq. (71) and (72), respectively.

$$m_{tot} = m_{sp} + m_{th} \tag{71}$$

$$c_{p,av} = \frac{c_{p,sp} m_{sp} + c_{p,th} m_{th}}{m_{tot}} \tag{72}$$

In Eq. (71) and (72), m_{sp} is the mass of the spacecraft, computed at each timestep depending on the geometry and on the instantaneous value of the wall thickness δ, while $c_{p,th}$ is the specific heat value of the thermite. Specific heat values are temperature dependent, with the main reference being NIST-JANAF tables [42] and ESA's ESTIMATE database [18].

The last ODE to be considered determines the value of the thickness δ and defines the ablation model. Being the mass of the spacecraft considered lumped, the external surface is assumed to regress uniformly, coherently with the random tumbling motion representation. The thickness variation is described by the following equation:

$$\dot{\delta} = \begin{cases} -\frac{\dot{Q}_{tot}}{h_{abl} \rho_{sp} S_{ext}} & \text{if } T_w > T_{melt} \wedge \dot{Q}_{tot} > 0 \\ 0 & \text{otherwise} \end{cases} \tag{73}$$

where h_{abl} is the heat of ablation of the spacecraft material, taken from [20], and ρ_{sp} its density. If δ reaches zero, complete demise is considered and the simulation is stopped.

5.7. Model verification

The results given by TRANSIT for three test cases have been compared to the ones given by two different commercial softwares, SAM [15] and SCARAB [14]. The results of SAM for the test cases have been taken by [20], as well as the initial conditions of the spacecraft. The results of SCARAB were, instead, the outcome of dedicated simulations performed at HTG GmbH. The initial conditions of the three different simulations, one for each geometry, are presented in Table 4. All these simulations do not imply the presence of a thermite charge on board. The geometry and material of each simulation is described in Table 5. Thermal properties that are dependent on temperature, in this set of simulation were considered constant and equal to the values reported in [20] to assure coherence between the simulations.

Table 4
Initial conditions of the re-entry simulations.

Variable	Value
Longitude [°]	0
Latitude [°]	0
Altitude [km]	120
Velocity [m/s]	7273
Flight path angle [°]	-2.612
Heading angle [°]	42.35
Temperature [K]	300

Table 5
Geometry and material of the re-entry simulations (model verification).

Test ID	Geometry	Dimensions [m]	Material
1	Sphere	$r_s = 0.5, \delta = 0.03$	Aluminium
2	Cylinder	$r_c = 0.5, l_c = 1, \delta = 0.03$	Aluminium
3	Box	$L = W = H = 1, \delta = 0.03$	Titanium

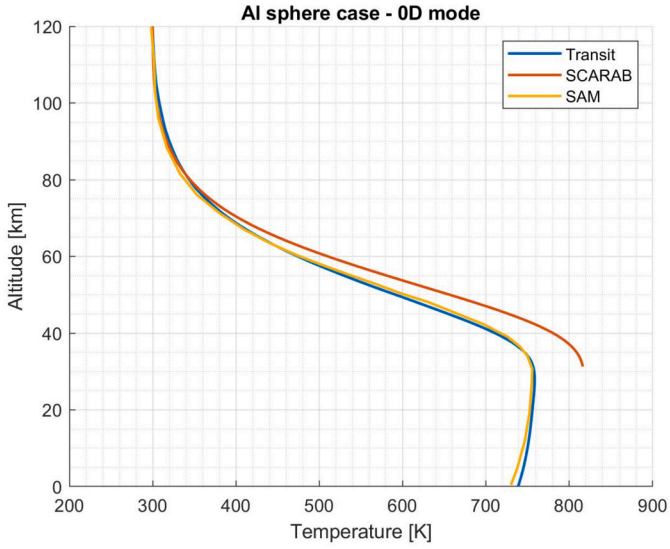

Fig. 4. Temperature profile of an aluminium sphere during re-entry, compared to SCARAB and SAM results (Test 1).

The results of the simulations are presented in Fig. 4–6. SCARAB simulations are stopped when the spacecraft starts to cool down, while TRANSIT simulations are continued up to landing to compare its behaviour with SAM. Excellent agreement can be seen with SAM code while, when compared to SCARAB, TRANSIT results show general coherence but with less accuracy. This behaviour is expected, as TRANSIT in 0D mode is an object-oriented code like SAM, while SCARAB uses a different approach, representing the geometry through panels [12]. Notice that the high number of modelling choices (e.g., correlations for heat load estimation) result in the impossibility of identifying a software package that is more conservative than the others in all conditions.

6. Numerical results

It is now possible to use the numerical model described in Section 5 and the experimental quantification of the heat transferred by the ther-

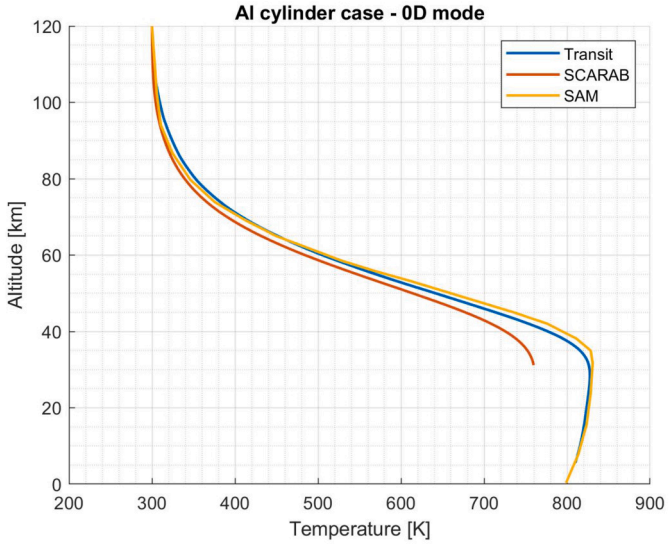

Fig. 5. Temperature profile of an aluminium cylinder during re-entry, compared to SCARAB and SAM results (Test 2).

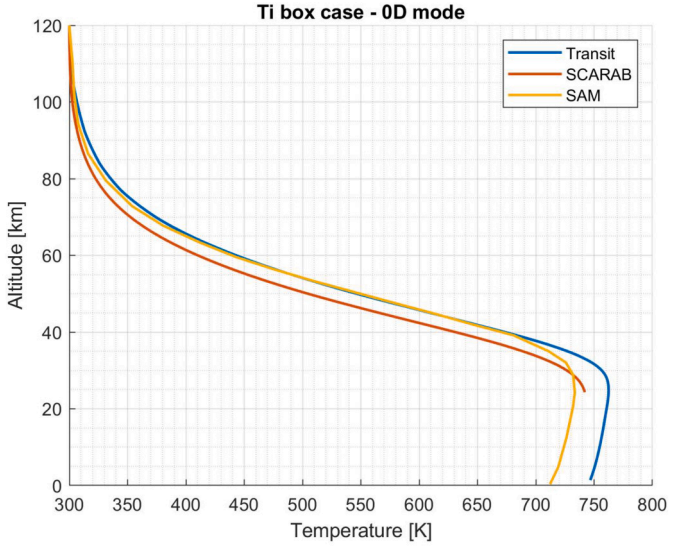

Fig. 6. Temperature profile of an titanium box during re-entry, compared to SCARAB and SAM results (Test 3).

mite to its vessel presented in Section 4 to preliminarily size a T4D application. An optimization analysis of the problem is necessary, as several parameters of the problem have a contrasting effect. For example, a higher mass of the charge implies a higher additional energy but a higher thermal inertia as well. A lower ignition temperature could result in a longer exposition of a smaller fragment, easier to demise, but this means that the thermite heat would not be released in correspondence to the highest aerodynamic heat flux during the descent. In addition, the effects on the ballistic coefficient are not easily quantifiable. For this reason, a genetic algorithm is used to determine the best set of parameters for the problem.

The initial conditions selected are the ones used in the model verification (Table 4). As for the geometric and material features, the ones used in Section 5.7 (Table 5) have been slightly changed and are presented in Table 6. In particular, for the cylinder case, the selected material for the optimization phase is stainless steel. The objective of this change is to evaluate the T4D performance for all the materials currently available in the model. In contrast to the validation section, in the following simulations the specific heat capacity is temperature dependent. Steel properties are taken from [42] and [18], as for aluminium and titanium. Moreover, the titanium box thickness was reduced to 0.025 m to ease demisability, while the internal dimensions were preserved. The original geometry was very close to the demisability limit, and therefore the titanium mass was downsized to let the genetic algorithm work properly.

Table 6
Geometry and material of the re-entry simulations (genetic algorithm optimization).

Test ID	Geometry	Dimensions [m]	Material
A	Sphere	$r_s = 0.5, \delta = 0.03$	Aluminium
B	Cylinder	$r_c = 0.5, l_c = 1, \delta = 0.03$	Steel
C	Box	$L = W = H = 0.99, \delta = 0.025$	Titanium

Table 7
Working variables, with relative lower and upper bounds, for genetic algorithm optimization of the re-entry thermite application.

Variable	Lower bound	Upper bound	Variable type
Profile [-]	1	5	Integer
Burning time [s]	1	100	Real
Thermite density [kg/m^3]	781	1095	Real
Filling factor [-]	0.1	1	Real
Temperature of ignition [K]	573	T_{melt}	Real

Table 8
Main parameters used in the genetic algorithm optimization.

Parameter	Parameter value
Number of generations	100
Population per generation	50
Number of parents mating	15

Lastly, thermite properties must be defined. Thermites are a quite flexible subset of energetic materials: compression, mechanical activation, fuel to oxidizer ratio and other parameters can be used to tune their properties. In this study the thermite formulation considered is a stoichiometric blend of Al+Fe_2O_3, so the specific enthalpy is fixed (see Section 3.2). Nevertheless, the density and the temperature of ignition of the mixture are tunable variables. A genetic algorithm is used to determine the best set of characteristics and a first sizing of the thermite charge for the reference cases shown in the verification of the model. The selected tool for this heuristic optimization is PyGAD [55], an open-source Python library. This library, ready to use for Python users, has been selected for its simplicity and versatility.

The boundaries of the working variables are described in Table 7. The Profile variable value identifies the different profiles discussed in Section 5, in the same order they have been presented. The lower and upper boundaries for the thermite density ρ_{th} were determined by a series of direct measures performed on Al+Fe_2O_3 thermite, after different mechanical activation processes. No compression of the thermite is considered. Lastly, the lower boundary for the temperature of ignition T_{ign} has been determined taking into account a temperature value that is normally beyond the usual thermal cycle of a satellite in LEO. The higher boundary for T_{ign} is the melting temperature of the spacecraft. This is justified by the assumption of passive ignition of the charge, determined by the heating of the spacecraft that acts as its vessel. The maximum temperature that it can reach is the melting temperature of its material, under the hypotheses of the model presented in Section 5.6. Therefore, the maximum value of T_{ign} should be the melting temperature of the spacecraft material.

Three genetic algorithm optimizations have been conducted, one for each geometry. The main parameters characterizing the genetic algorithm are shown in Table 8. Notice that mutation and crossover settings

Table 9
Outcome of the three optimizations considering different geometries and materials.

Test ID	Geometry	Material	Fitness	Variable	Variable Value
A	Sphere	Aluminium	4.11	Profile [-]	Gaussian
				Burning time [s]	10.16
				Thermite density [kg/m^3]	861.10
				Filling factor [-]	0.16
				Temperature of ignition [K]	639.44
B	Cylinder	Stainless steel	1.67	Profile [-]	Gaussian
				Burning time [s]	24.38
				Thermite density [kg/m^3]	1004.48
				Filling factor [-]	0.97
				Temperature of ignition [K]	584.44
C	Box	Titanium	0.94	Profile [-]	Gaussian
				Burning time [s]	27.69
				Thermite density [kg/m^3]	990.20
				Filling factor [-]	0.81
				Temperature of ignition [K]	653.38

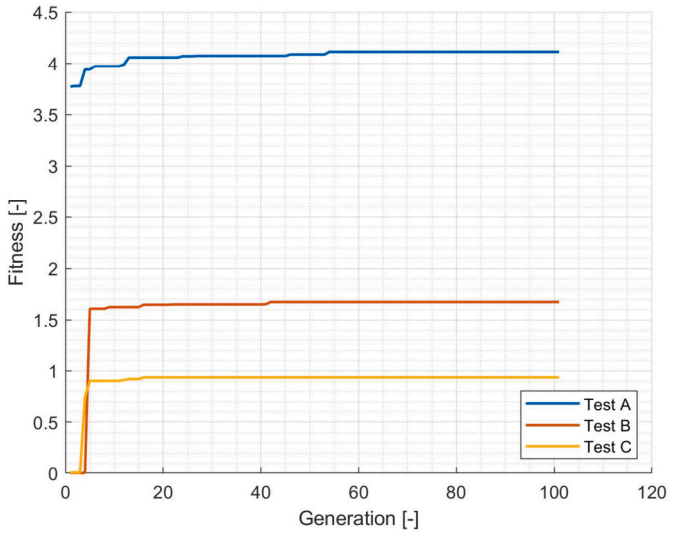

Fig. 7. Fitness parameter evolution with respect to the generation number for the three test cases considered.

used in these simulations were the default values that can be found in PyGAD documentation [55].

A choice of paramount importance for a correct genetic algorithm optimization is the definition of a suitable objective function, hereby named f. For this study, it has been defined as follows:

$$f = \frac{1}{m_f + \frac{m_{th}}{m_{sp}} + 0.0000001} \tag{74}$$

where m_f is the mass of the spacecraft at the end of the simulation, computed considering the residual thickness, and m_{th} and m_{sp} are the mass of the thermite charge on board and the initial spacecraft mass, respectively. The value assumed by the function f for a given set of variables, bounded as described in Table 7, is the fitness of that set. The genetic algorithm tries to maximize the fitness, giving the conditions to minimize the thermite mass on board, maintaining complete demise. The outcome of the three optimization is shown in Table 9. In Fig. 7 the value of the fitness function at the different generations for the three test cases is drawn. Since this parameter reaches a steady value, the optimization is considered successful.

As total demise was registered for all three cases, the fitness value is actually the maximum ratio between m_{sp} and m_{th} that has been determined. It is important to highlight that, during a real T4D application, this mass ratio would refer to the robust components that would reach the ground and not to the whole spacecraft: this could imply a significant weight reduction with respect to the fuel mass needed for a controlled re-entry. As expected, each gram of steel or titanium requires a significantly higher mass of thermite to be demised, with respect to what is necessary for aluminium. In this study, filling factor and thermite density are treated as different genes. Their role in the thermite mass computation is the same: the important parameter, actually, is their product. Nevertheless, considering these values as separated genes could be important in future versions of TRANSIT, should porosity or partial filling effects be implemented.

What is more interesting to notice is the trend in profile, burning time, and temperature of ignition selection. In all the three cases, the Gaussian profile characterizes the best solution found by the algorithm. As for the burning time and the temperature of ignition, at a first glance their values seem to lay in the middle of the consented boundaries. However, the mathematical description of this profile implies that the 95% of the heat is released in one twentieth of the burning time t_{th}. Therefore, the results shown in Table 9 indicate that a very brief heat release is beneficial.

Moreover, analyzing the best cases obtained by the genetic algorithm optimization in case of failed thermite ignition can give an useful insight. Fig. 8a–10a show the temperature of ignition and of the thermite heat release peak, for successful ignition, superposed to the temperature profile of the best solution in case of failed ignition, for the three different geometries. The failed ignition case is chosen as it represents the best case “without” the thermite contribution to the thermal history. It is evident that the burning time registered for the best solutions referring to the Gaussian profile is actually a delay imposed to the fast heat release. This strategy approaches the maximum temperature reached by the re-entering object. This result suggests that the best performance is given by a brief, intense heat release happening at the maximum temperature during the re-entry, as it can be seen in Fig. 8b–10b. The effect of the thermite charge can be seen as well in Fig. 8c–10c, where the thickness of the spacecraft is drawn along the re-entry.

This beneficial effect of a brief and intense heat release was already observed in [28], in which it was initially understood using a previous version of the hereby presented numerical model and a simple parametric analysis. The heuristic optimization strengthens this insight. A late ignition, close to the maximum temperature during the re-entry, helps to maintain the temperature difference between the hot air after the shock and the body high for a long period. Moreover, a late decrease in mass implies higher velocities, hence leading to a higher heat flux. However, it is important to remember that these considerations apply to a monolithic re-entering object. If the target of a T4D application is a structural joint with the objective of provoking controlled fragmentation, an early ignition is expected to be beneficial, as it would result in an increase of exposed surface area.

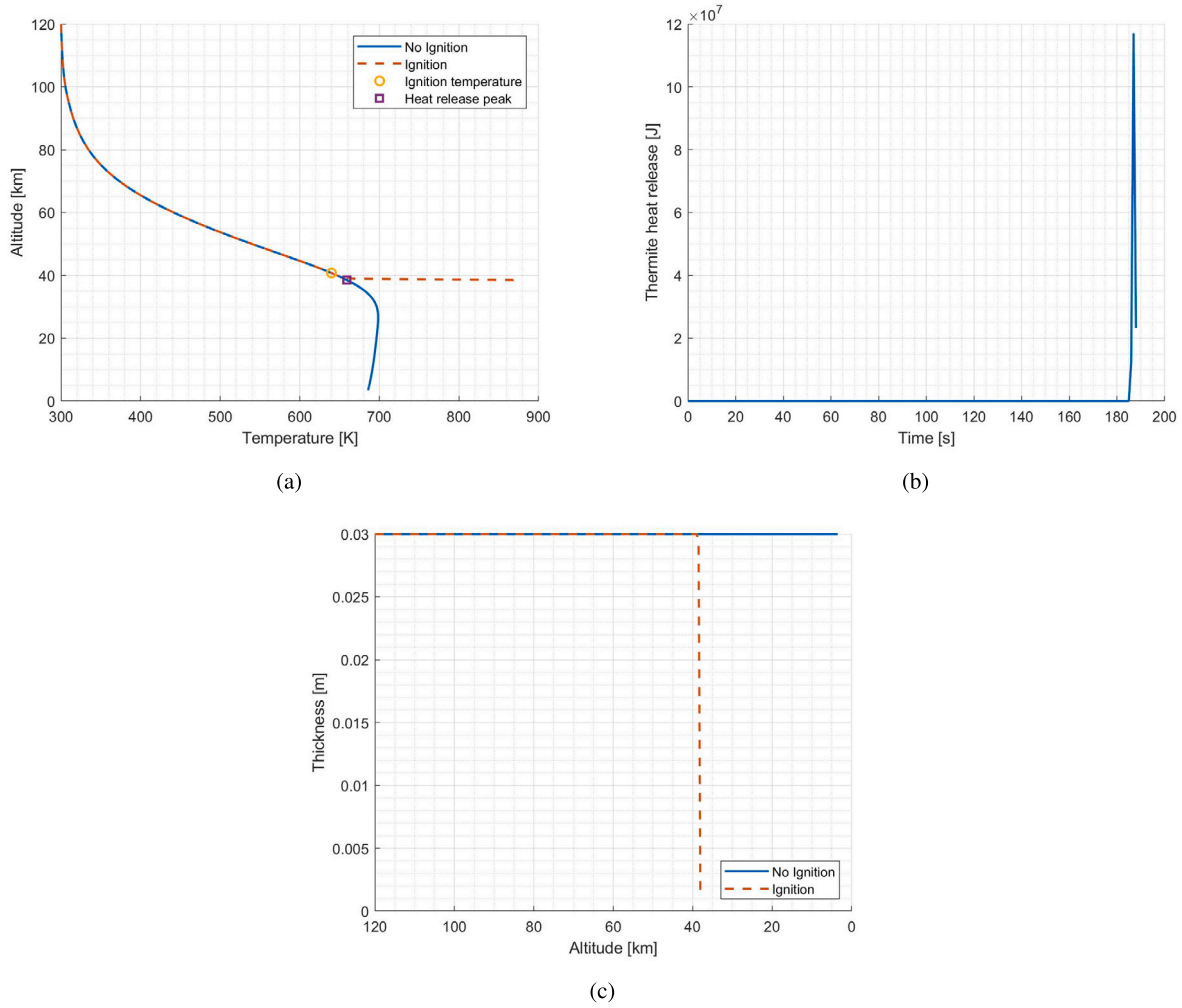

Fig. 8. a) Temperature profile for an aluminium sphere containing a thermite charge as described in Table 9 (Test A), in case of failed ignition (blue solid line) and successful ignition (red dashed line). Ignition temperature and thermite heat peak release for the best solution are shown. b) Thermite heat release for the best solution. c) Thickness of the aluminium sphere along the re-entry, in case of failed ignition (blue solid line) and successful ignition (red dashed line). (For interpretation of the colours in the figure(s), the reader is referred to the web version of this article.)

7. Conclusions

This paper presented the first results of Politecnico di Milano regarding the use of thermitic exothermic reaction to aid spacecraft demise during re-entry.

Firstly, an experimental quantification of the heat transferred by a confined thermite charge to its vessel has been provided. The considered thermite was a stoichiometric mixture of Aluminum and Iron (III) Oxide (Fe_2O_3), placed in a steel cylindrical vessel. The experimental quantification showed a thermite performance of about 60% with respect to the theoretical heat release, significantly higher than the value previously registered in literature (around 10%) [41]. This difference was attributed mainly to the different geometry, that in the hereby studied configuration is closed. Another important remark on the experimental results presented in this paper is the effectiveness of the mechanical activation, that granted a tunable thermite ignition temperature, in this case lowered to the operating range of the hot air blower employed in the experiments (maximum temperature of 900°C).

Secondly, the TRANSIT numerical model, with its 0D approach, has been presented in detail. This object-oriented code has been verified with respect to two commercial softwares (SAM and SCARAB), showing good agreement for all the cases investigated. A genetic algorithm optimization has been used to get insight on the thermite to spacecraft mass ratio for the three studied cases. While the optimized results cannot be extended to any arbitrary geometric and re-entry condition, as the final result is deeply influenced by the thermal load acting on the re-entering spacecraft, the presented method can be used to determine the convenience of a T4D application for a specific spacecraft. Moreover, the obtained results suggest that a late ignition, happening in the proximity of the maximum temperature during the re-entry and provoking a brief and intense heat release, is more beneficial than other thermal profiles. This strategy assures to maintain for a longer time a high ballistic coefficient and a high temperature difference between the re-entering body and the hot air after the shock. Both these conditions concur to a higher heat flux on the spacecraft.

An extension of the study hereby presented with panel-based software could provide useful insights. For this scope, a new version of TRANSIT is currently under development, using a simplified panel-based approach. Furthermore, a more detailed model (e.g., SCARAB) could confirm and extend these results to spacecraft fragmentation. Moreover, an application of the presented methodology to real cases would provide useful information to evaluate the possible performance of a T4D approach. Finally, a finer quantification of the heat transfer efficiency of a thermite charge to its vessel in relevant conditions (i.e., in a plasma wind tunnel) would help to characterize the energetic material behaviour and to improve the sizing methodology discussed in this paper. Such a study could as well represent an independent experimental validation point for TRANSIT, that could limit the need for comparison

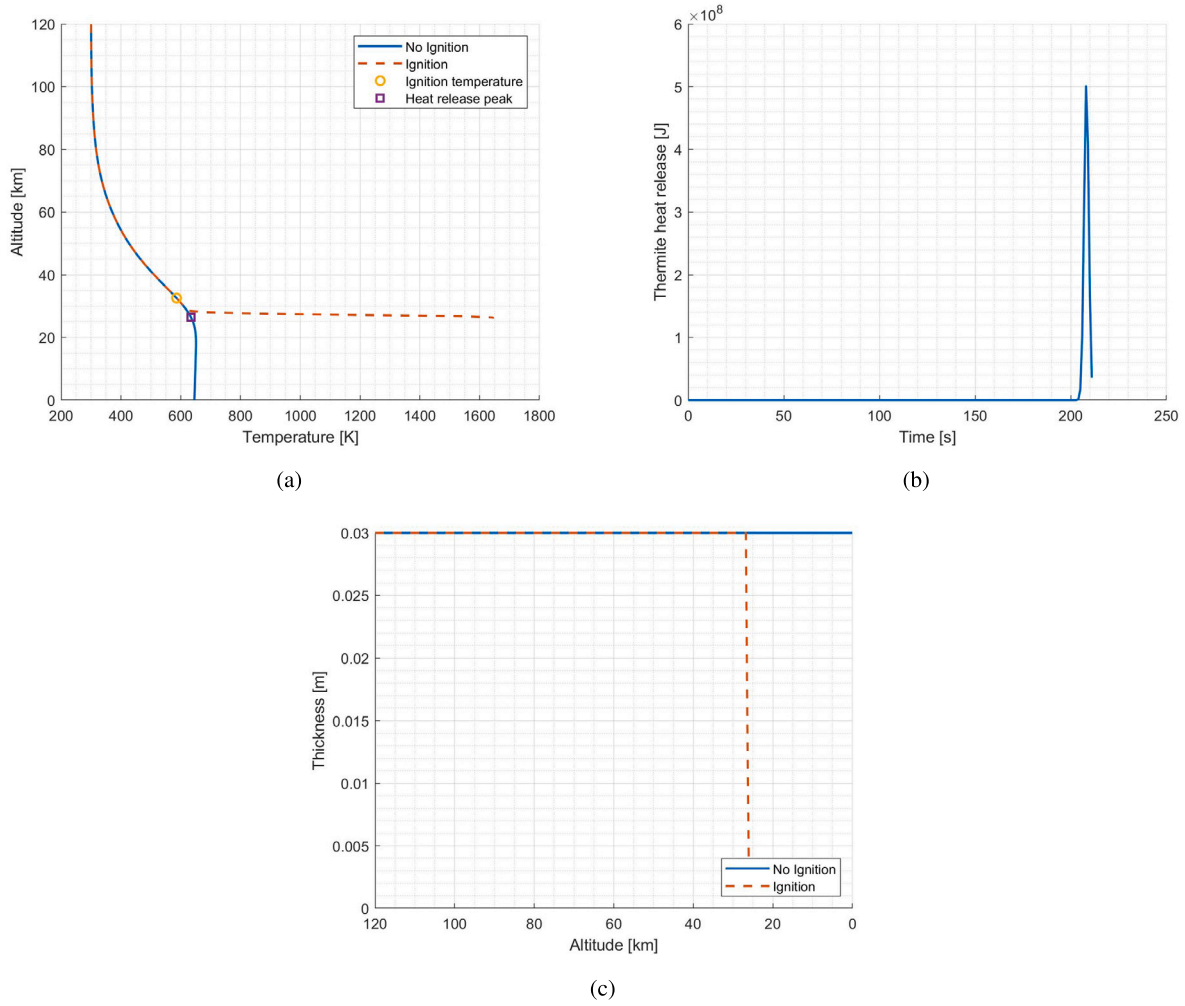

Fig. 9. a) Temperature profile for a steel cylinder containing a thermite charge as described in Table 9 (Test B), in case of failed ignition (blue solid line) and successful ignition (red dashed line). Ignition temperature and thermite heat peak release for the best solution are shown. b) Thermite heat release for the best solution. c) Thickness of the steel cylinder along the re-entry, in case of failed ignition (blue solid line) and successful ignition (red dashed line). (For interpretation of the colours in the figure(s), the reader is referred to the web version of this article.)

with established commercial codes. A computational fluid dynamics approach, as well, could be a valuable extension of this work, always in the same perspective.

CRediT authorship contribution statement

A. Finazzi: Conceptualization, Formal analysis, Investigation, Methodology, Software, Validation, Writing – original draft, Writing – review & editing. **P. Finocchi:** Formal analysis, Investigation, Validation. **S. Carlotti:** Writing – review & editing. **F. Maggi:** Conceptualization, Funding acquisition, Resources, Supervision, Writing – review & editing.

Declaration of competing interest

The authors declare the following financial interests/personal relationships which may be considered as potential competing interests:

Filippo Maggi reports financial support was provided by European Space Agency. Filippo Maggi reports a relationship with ReActive Powder Technology that includes: board membership.

Data availability

Data will be made available on request.

Acknowledgements

The research presented in this paper has been partially supported by ESA-TRP SPADEXO project, contract number ESA AO/1-10812/21/NL/MG. HTG GmbH is gratefully acknowledged for the dedicated SCARAB simulations.

Appendix A. Hot blower flow characterization

The hot air blower used to provoke the thermite ignition in the tests presented in this paper is a Leister Hotwind “S”. The flow generated by this tool has been characterized with an Alnor Velometer Anemometer Series 6000 and a 2 mm type K thermocouple. The flow velocity and temperature were measured both in the horizontal (x) and vertical (y) directions at 0.5 cm from the blower outlet. In a similar manner, the measure was performed along the normal direction (z), in correspondence of the centre of the outlet. Data were recorded after stabilization of sensor readings to steady state condition.

Velocity values displayed by the velometer were corrected to account for high flow temperature using Eq. (A.1).

$$v_r = \sqrt{\frac{\rho_d}{\rho_r}} v_d \tag{A.1}$$

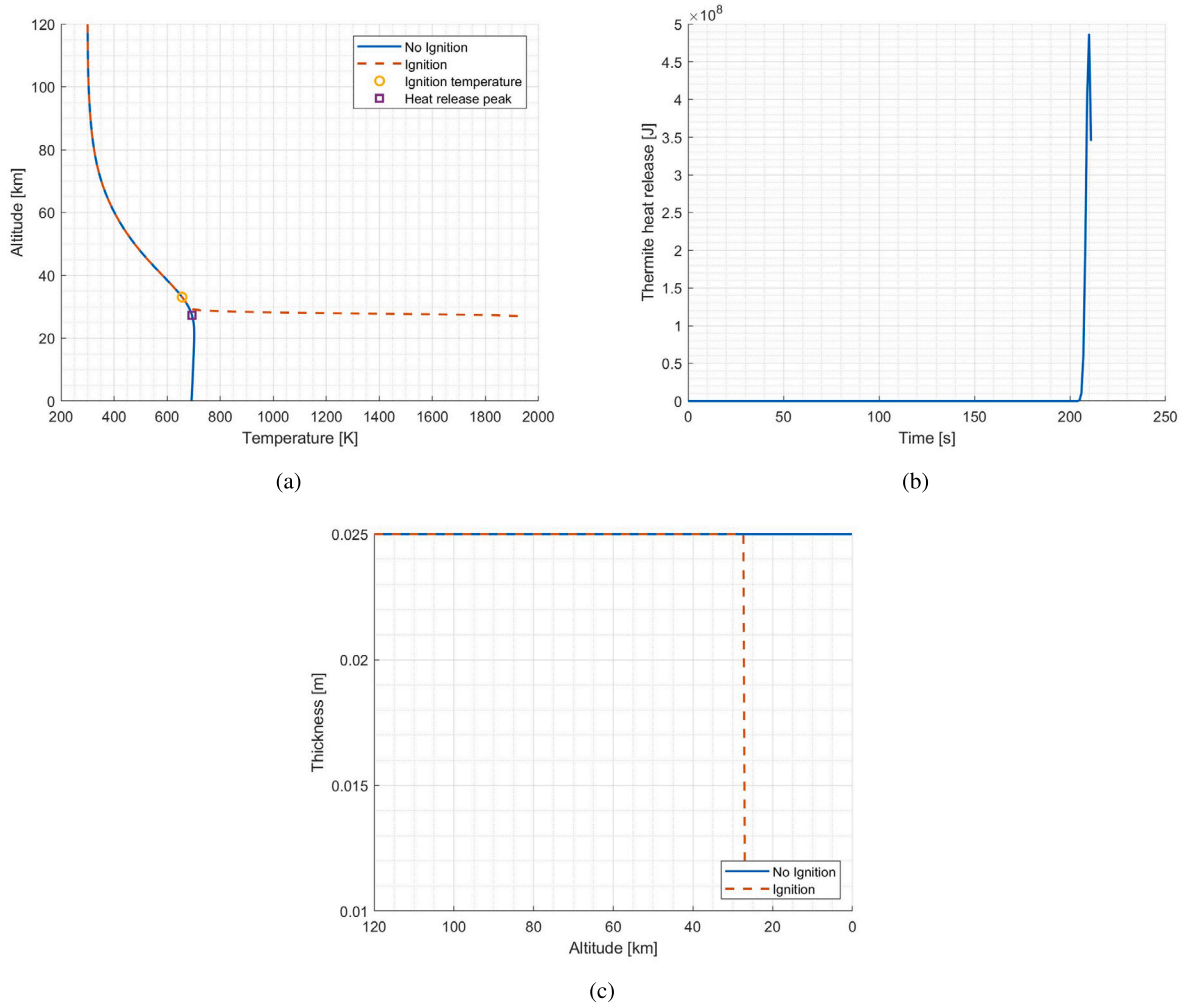

Fig. 10. a) Temperature profile for a titanium box containing a thermite charge as described in Table 9 (Test C), in case of failed ignition (blue solid line) and successful ignition (red dashed line). Ignition temperature and thermite heat peak release for the best solution are shown. b) Thermite heat release for the best solution. c) Thickness of the titanium box along the re-entry, in case of failed ignition (blue solid line) and successful ignition (red dashed line). (For interpretation of the colours in the figure(s), the reader is referred to the web version of this article.)

In Eq. (A.1), v_r and ρ_r are respectively the corrected velocity value and the air density at high temperature, while v_d and ρ_d are respectively the displayed velocity and the air density under standard conditions. The density at high temperature was computed considering the ambient pressure and under the hypothesis of ideal gas. Moisture was not taken into account. The outcome of the flow characterization is shown in Fig. A.11.

References

[1] AA. VV., ESA's Annual Space Environment Report, European Space Agency Space Debris Office, Issue 6, Darmstadt, Germany, 2022.

[2] European Space Agency, Working together towards zero debris: a concurrent study is coming, https://blogs.esa.int/cleanspace/2022/07/28/zero-debris-cdf-study/. (Accessed 29 October 2022).

[3] AA. VV., IADC Space Debris Mitigation Guidelines, Inter-Agency Space Debris Coordination Committee, Revision 2 2020.

[4] R. Seiler, G. Smet, Exothermic reaction aided spacecraft demise during re-entry, Patent EP 3604143A1, 2018.

[5] D. Dihlan, P. Omaly, Élement de véhicule spatial a capacité d'autodestruction ameliorée et procedure de fabrication d'un tel elément, Patent FR 2975080B1, 2011.

[6] K.A. Monogarov, A.N. Pivkina, L.I. Grishin, Yu.V. Frolov, D. Dilhan, Uncontrolled re-entry of satellite parts after finishing their mission in LEO: titanium alloy degradation by thermite reaction energy, Acta Astronaut. 135 (2017) 69–75.

[7] T. Schleutker, A. Guelhan, B. Esser, T. Lips, Exothermic Reaction Aided Spacecraft Demise - Proof of Concept Testing – Final Report, Contract No. 4000126547/19/NL/AR/ig, Issue 1, Revision 2, 2019.

[8] AA. VV., Tri-Agency Reliability Engineering Guidance: Post Mission Disposal and Extension Assessment, ESA-TECQQD-TN-025375 / CAA-2021025 / NASA/SP-20210024973, ESA, JAXA and NASA, January 2022.

[9] L. Visagie, V. Lappas, S. Erb, Drag sails for space debris mitigation, Acta Astronaut. 159 (2015) 65–75.

[10] R.L. Forward, R.P. Hoyt, C.W. Uphoff, Terminator tether: a spacecraft deorbit device, J. Spacecr. Rockets 37 (2) (March-April 2000).

[11] AA. VV., Final Report - Upgrade of DRAMA's Spacecraft Entry Survival Analysis Codes, Contract No. 4000115057/15/D/SR, Issue 3, Revision 1.0.2, Hyperschall Technologie Goettingen GmbH, December 20, 2019.

[12] T. Lips, V. Wartemann, G. Koppenwallner, H. Klinkrad, D. Alwes, J. Dobarco-Otero, R.N. Smith, R.M. DeLaune, W.C. Rochelle, N.L. Johnson, Comparison of ORSAT and SCARAB re-entry survival results, in: Proceedings of the Fourth European Conference on Space Debris, Darmstadt, Germany, 18–20 April, 2005.

[13] AA. VV., DIVE - Guidelines for Analysing and Testing the Demise of Man Made Space Objects During Re-entry, Technical Note ESA-TECSYE-TN-018311, European Space Agency, European Space Research and Technology Centre, Noordwijk, The Netherlands, May 5, 2020.

[14] G. Koppenwallner, B. Fritsche, T. Lips, H. Klinkrad, SCARAB - a multi-disciplinary code for destruction analysis of space-craft during re-entry, in: 5th European Symposium on Aerothermodynamics for Space Vehicles, Cologne, Germany, 8–11 November, 2005.

[15] J. Beck, I. Holbrough, J.A. Merrifield, N. Joiner, S. Bainbridge, Progress in hybrid Spacecraft/Object Oriented destructive re-entry modelling using the SAM code, in: Proc. 7th European Conference on Space Debris, Darmstadt, Germany, 18–21 April, 2017.

[16] M. Spel, J. Dumon, E. Constant, P. Van Hauwaert, S. Galera, J. Annaloro, Demisability study of industrial test cases with the Spacecraft-Oriented code PAMPERO,

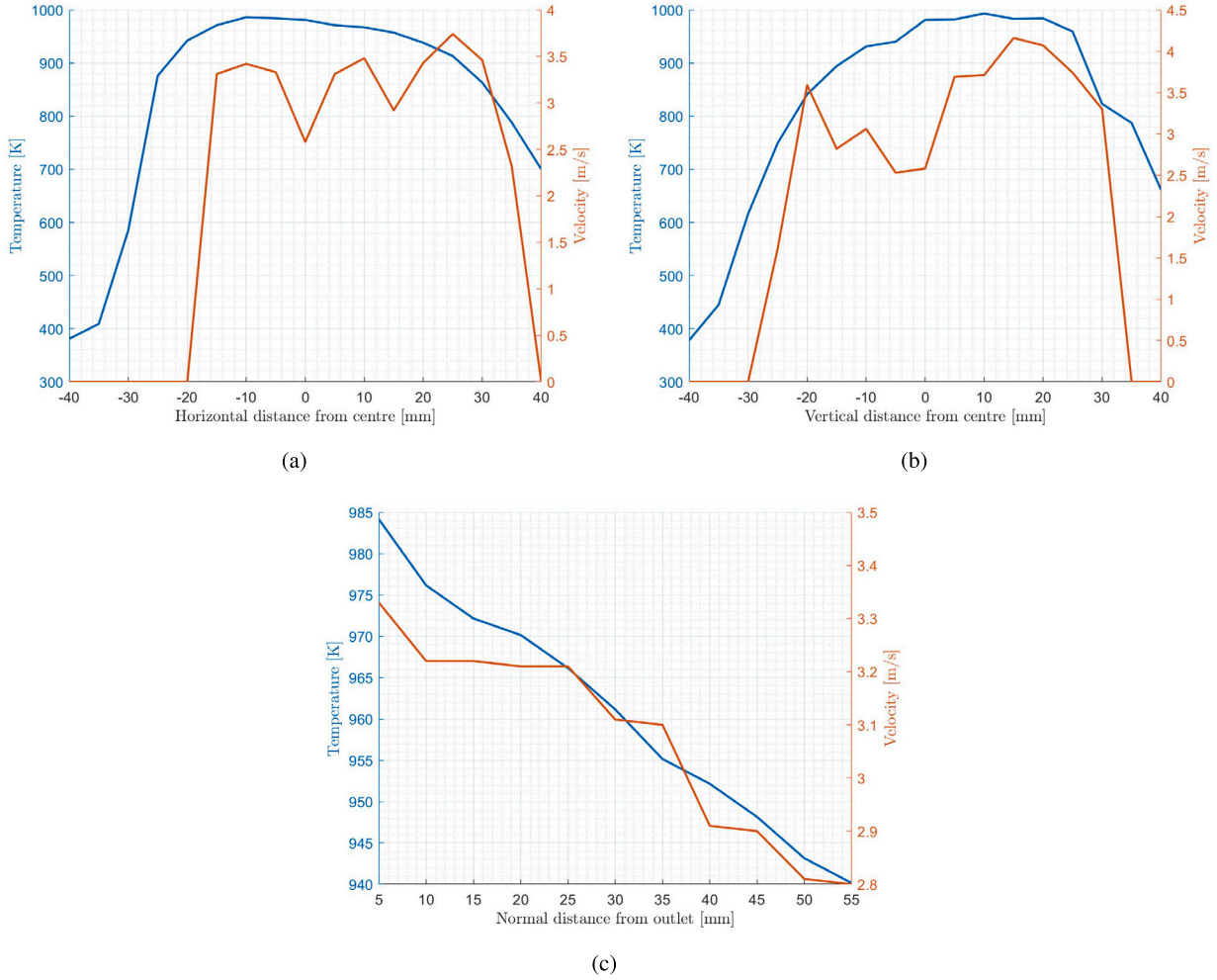

Fig. A.11. Temperature and velocity patterns at 5 mm from the outlet of the hot air blower. Outlet diameter is 60 mm.

in: Proc. 8th European Conference on Space Debris (virtual), Darmstadt, Germany, 20–23 April, 2021.
[17] R.G. Stern, Reentry Breakup and Survivability Characteristics of the Vehicle Atmospheric Survivability Project (VASP) Vehicles, The Aerospace Corporation, Report No. TR-2008(8506)-3, 5 August, 2008.
[18] Anon., European Space maTerIal deMisability dATabasE, European Space Agency Space Debris Office, https://estimate.sdo.esoc.esa.int/. (Accessed 21 November 2022).
[19] S.H. Park, S. Mischeler, P. Leyland, Re-entry analysis of critical components and materials for demise-for-demise techniques, Adv. Space Res. 68 (2021) 1–24.
[20] M. Trisolini, Space System Design for Demise and Survival, PhD Thesis, University of Southampton, Faculty of Engineering and the Environment, Department of Astronautics, 2018.
[21] Anon., Demisable metallic tank, in: ESA CleanSpace Industrial Days, MT Aerospace AG, European Space Research and Technology Centre, Noordwijk, The Netherlands, May 23–27, 2016.
[22] Anon., Demisable high pressure tanks for LEO Satcoms, European Space Agency, https://artes.esa.int/projects/demisable-high-pressure-tanks-leo-satcoms. (Accessed 14 April 2023).
[23] Anon., Aluminium propellant tanks, Nammo Space, https://www.nammo.com/product/aluminium-propellant-tank/. (Accessed 14 April 2023).
[24] T. Lips, B. Fritsche, R. Kanzler, T. Schleutker, A. Gülhan, B. Bonvoisin, T. Soares, G. Sinnema, About the demisability of propellant tanks during atmospheric re-entry from LEO, J. Space Saf. Eng. 4 (2017) 99–104.
[25] M.A. Vidal Urriza, A. Caiazzo, J. Beck, T. Lips, T. Schleutker, M. Weihreter, A. Sita, A. Iffly, S. Heinrich, Design For Containment techniques to reduce spacecraft re-entry footprint, in: 2nd International Conference on Flight Vehicles, Aerothermodynamics and Re-entry Missions & Engineering, Heilbronn, Germany, June 19–23, 2022.
[26] S.H. Fischer, N.C. Grubelich, Theoretical energy release of thermites, intermetallics, and combustible metals, in: 24th International Pyrotechnics Seminar, Monterey, CA, July, 1998.
[27] L.L. Wang, Z.A. Munir, Y.M. Maximov, Thermite reactions: their utilization in the synthesis and processing of materials, J. Mater. Sci. 28 (1993) 3693–3708.
[28] A. Finazzi, F. Maggi, C. Paravan, L. Galfetti, S. Dossi, A. Murgia, T. Lips, G. Smet, Thermite-for-Demise (T4D): concept definition for exothermic reaction-aided spacecraft demise during re-entry, in: 9th European Conference for Aeronautics and Space Sciences, Lille, France, 27 June – 01 July, 2022.
[29] T.M. Klapoetke, Chemistry of High Energy Materials, 2nd edition, Walter de Gruyter GmbH & Co. KG, Berlin/Boston, 2012.
[30] S. Dossi, C. Paravan, F. Maggi, L. Galfetti, Enhancing micrometric aluminum reactivity by mechanical activation, in innovative energetic materials: properties, combustion performance and application, in: Innovative Energetic Materials: Properties, Combustion Performance and Application, Springer Nature, 2020, pp. 17–44.
[31] S. Dossi, C. Paravan, F. Maggi, L. Galfetti, Novel activated metal powders for improved hybrid fuels and green solid propellants, in: 52nd AIAA/SEA/ASEE Joint Propulsion Conference, Salt Lake City, UT, USA, July 25–27, 2016.
[32] S. Dossi, F. Maggi, Ignition of mechanically activated aluminum powders doped with metal oxides, Propellants Explos. Pyrotech. 44 (10) (2019) 1312–1318.
[33] C. Suryanarayana, Mechanical alloying and milling, Prog. Mater. Sci. 46 (2001) 1–184.
[34] C. Paravan, A. Verga, F. Maggi, L. Galfetti, Accelerated ageing of micron- and nano-sized aluminum powders: metal content, composition and non-isothermal oxidation reactivity, Acta Astronaut. 158 (2019) 397–406.
[35] C. Wang, J. Xu, Y. Shen, Y. Wang, T. Yang, Z. Zhang, F. Li, R. Shen, Y. Ye, Thermodynamics and performance of Al/CuO nanothermite with different storage time, Def. Technol. 17 (3) (2021) 741–747.
[36] A. Estève, G. Lahiner, B. Julien, S. Vivies, N. Richard, C. Rossi, How thermal aging affects ignition and combustion properties of reactive Al/CuO nanolaminates: a joint theoretical/experimental study, Nanomaterials 10 (2020) 2087.
[37] P.S. Wang, Thermally induced surface changes in aluminium-iron oxide thermites, J. Mater. Sci. 20 (1985) 648–653.
[38] A.M. Taylor, J.J. Granier, D.E. Wilson, D.R. Barnette, Torch for cutting or perforation, Patent US 925975 B1, 2016.
[39] C.A. Crane, E.S. Collins, M.L. Pantoya, B.L. Weeks, Nanoscale investigation of surfaces exposed to a thermite spray, Appl. Therm. Eng. 31 (2011) 1286–1292.

[40] E.S. Collins, M.L. Pantoya, M.A. Daniels, D.J. Prentice, E.D. Steffler, S.P. D'Arche, Heat flux analysis of a reacting thermite spray impingent on a substrate, Energy Fuels 26 (2012) 1621–1628.
[41] C. Crane, M. Pantoya, J. Dunn, Quantifying energy transfer from a reacting thermite to a target using infrared diagnostics, in: Proceedings of the ASME 2009 Heat Transfer Summer Conference, San Francisco, California, USA, July 19–23, 2009.
[42] Y.S. Touloukian, E.H. Buyko, Thermophysical Properties of Matter - the TPRC Data Series - vol. 4. Specific Heat - Metallic Elements and Alloys, Purdue University, West Lafayette, IN, USA, 1971.
[43] S. Rafano Carná, R. Bevilacqua, High fidelity model for the atmospheric re-entry of CubeSats equipped with the Drag De-Orbit Device, Acta Astronaut. 156 (2019) 134–156.
[44] J.M. Picone, A.E. Hedin, D.P. Drob, A.C. Aikin, NRL-MSISE-00 empirical model of the atmosphere: statistical comparisons and scientific issues, J. Geophys. Res. 107 (A12) (2003), SIA 15-1:15-16.
[45] A. Tewari, Atmospheric and Space Flight Dynamics - Modeling and Simulation with MATLAB and Simulink, Birkhäuser, Boston, 2007.
[46] J.D. Anderson Jr., Hypersonic and High Temperature Gas Dynamics, 2nd edition, American Institute of Aeronautic and Astronautics, Reston, Virginia, USA, 2006.
[47] D.J. Masson, D.N. Morris, D.E. Bloxsom, Measurements of Sphere Drag from Hypersonic Continuum to Free-Molecule Flow, RAND Corporation, Santa Monica, CA, USA, 1960.
[48] R.D. Klett, Drag coefficients and heating ratios for right circular cylinders in free-molecular and continuum flow from Mach 10 to 30, Report SC-RR-64-2141, Sandia Laboratory, Albuquerque, 1964.
[49] W.P. Hallmann, D.M. Moody, Trajectory Reconstruction and Heating Analysis of Columbia Composite Debris Pieces, The Aerospace Corporation, Cambridge, MA, USA, 2005.
[50] J.C. Tannehill, P.H. Mugge, Improved curve fits for the thermodynamic properties of equilibrium air suitable for numerical computation using time-dependent or shock-capturing methods, NASA CR-2470, Washington D.C., USA, 1974.
[51] L.T. De Luca, Energetic problems in aerospace propulsion - Notes for students, Grafiche GSS, Revised and Extended Preliminary Edition, Bergamo, Italy, 2008.
[52] Anon., NIST-JANAF Tables (PDF), National Institute of Standards and Technology, U.S. Department of Commerce, https://janaf.nist.gov/janaf4pdf.html. (Accessed 9 November 2022).
[53] J.A. Fay, F.R. Riddel, Theory of stagnation point heat transfer in dissociated air, J. Aerosp. Sci. 25 (2) (1958) 73–85.
[54] H. Legge, Hypersonic approximations for heat transfer and shear stress applied to continuum and rarefied plume impingement, Tech. Rep., DFVLR-ib 222:237 A23, Deutsche Forschungs- und Versuchsanstalt für Luft- und Raumfahrt, 1987.
[55] A.F. Gad, PyGAD: an intuitive genetic algorithm Python library, arXiv:2106.06158, 2021.